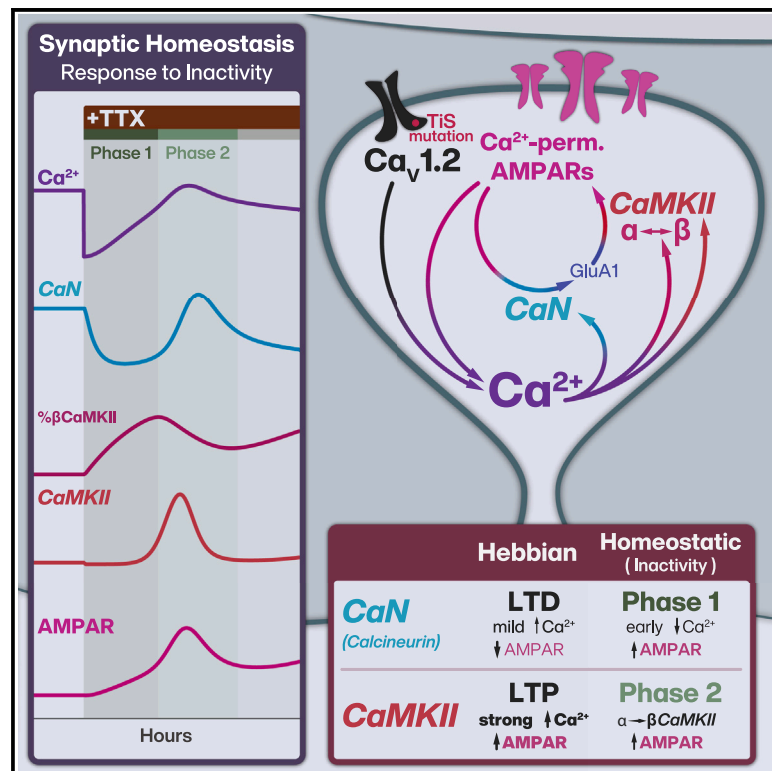# Synaptic homeostasis transiently leverages Hebbian mechanisms for a multiphasic response to inactivity

Graphical abstract

Authors

Simón(e) D. Sun, Daniel Levenstein,
Boxing Li, ..., John Rinzel,
György Buzsáki, Richard W. Tsien

Correspondence

richard.tsien@nyulangone.org

In brief

Sun et al. find that prolonged spike blockade elicits fluctuating increases in synaptic strength that transiently involves mechanisms linked to long-term potentiation and depression. Using experimental and computational approaches, they describe how synapses use Hebbian and homeostatic elements to adapt to changing activity levels while retaining the capacity for plasticity.

Highlights

- Inactivity-induced synaptic homeostasis *in vitro* is non-monotonic and multiphasic

- L-type Ca^{2+} channels shape the dynamic response to prolonged inactivity

- CaMKII and CaN act on glutamate receptors to stabilize postsynaptic Ca^{2+} levels

- Regulating CaMKII Ca^{2+} sensitivity *in silico* maintains synaptic responsiveness

CellPress

Article

Synaptic homeostasis transiently leverages Hebbian mechanisms for a multiphasic response to inactivity

Simón(e) D. Sun,[1,2,3] Daniel Levenstein,[1,2,4] Boxing Li,[2,5] Nataniel Mandelberg,[2] Nicolas Chenouard,[2,6] Benjamin S. Suutari,[1,2] Sandrine Sanchez,[2] Guoling Tian,[2] John Rinzel,[1] György Buzsáki,[2] and Richard W. Tsien[1,2,7,*]

[1]Center for Neural Science, New York University, New York, NY 10003, USA
[2]Department of Neuroscience and Physiology, Neuroscience Institute, New York University Langone Health, New York, NY 10016, USA
[3]Cold Spring Harbor Laboratory, Cold Spring Harbor, NY 11724, USA
[4]Montreal Neurological Institute, Department of Neurology and Neurosurgery, McGill University, 3810 University Street, Montreal, QC, Canada
[5]Neuroscience Program, Guangdong Provincial Key Laboratory of Brain Function and Disease, Zhongshan School of Medicine and the Fifth Affiliated Hospital, Sun Yat-sen University, Guangzhou 510810, China
[6]Sorbonne Université, INSERM U1127, UMR CNRS 7225, Institut du Cerveau (ICM), 47 bld de l'hôpital, 75013 Paris, France
[7]Lead contact
*Correspondence: richard.tsien@nyulangone.org
https://doi.org/10.1016/j.celrep.2024.113839

SUMMARY

Homeostatic regulation of synapses is vital for nervous system function and key to understanding a range of neurological conditions. Synaptic homeostasis is proposed to operate over hours to counteract the destabilizing influence of long-term potentiation (LTP) and long-term depression (LTD). The prevailing view holds that synaptic scaling is a slow first-order process that regulates postsynaptic glutamate receptors and fundamentally differs from LTP or LTD. Surprisingly, we find that the dynamics of scaling induced by neuronal inactivity are not exponential or monotonic, and the mechanism requires calcineurin and CaMKII, molecules dominant in LTD and LTP. Our quantitative model of these enzymes reconstructs the unexpected dynamics of homeostatic scaling and reveals how synapses can efficiently safeguard future capacity for synaptic plasticity. This mechanism of synaptic adaptation supports a broader set of homeostatic changes, including action potential autoregulation, and invites further inquiry into how such a mechanism varies in health and disease.

INTRODUCTION

Synaptic plasticity is thought to be a key biological substrate of learning, memory, and neural circuit development. It is theorized that two forms of plasticity—(1) Hebbian positive feedback to strengthen active synapses (long-term potentiation [LTP]) and diminish less active ones (long-term depression [LTD]), and (2) homeostatic negative feedback to maintain functional stability—enable neurons to integrate recent activity changes without veering into extreme hypo- or hyperactivity. There has been considerable interest in understanding the basis of synaptic adaptation to inactivity, its temporal dynamics, molecular underpinnings, and functional implications, based on *in vitro*,[1] *in vivo*, and *ex vivo* approaches.[2,3] Despite this effort, including many mechanistic studies *in vitro*, precisely how biochemical and cell biological processes merge into a homeostatic feedback system has not been fully settled.

Although Hebbian and homeostatic plasticity are typically conceptualized as distinct processes, the requisite molecular players exhibit considerable overlap.[4] For example, the calcium

(Ca^{2+})/calmodulin (CaM)-dependent kinase CaMKII and phosphatase calcineurin (CaN) are primarily associated with LTP/LTD,[5–8] but are also involved in homeostatic responses.[9–11] L-type voltage-gated Ca^{2+} channels (LTCCs), which regulate CaN and CaMKII,[12,13] are involved in both Hebbian[14–16] and homeostatic[17,18] changes. Such divisions are even murkier when linking α-amino-3-hydroxy-5-methyl-4-isoxazolepropionic acid receptor (AMPAR) subunits to certain plasticity paradigms.[19,20] Ca^{2+}-permeable AMPARs (CPARs), although often associated with LTP,[21–24] are also involved in homeostatic plasticity,[10,25] and homeostatic feedback can change the expression levels of several AMPAR subunits—GluA1[26–29] and GluA2/3.[29–31] Curiously, each of these players operate on different timescales, ranging from seconds[32–34] to minutes[15,35] to hours.[36,37–39] Conceptually distinguishing Hebbian and homeostatic plasticity requires the clarification of how multifunctional players are differentially engaged when these forms of neuronal plasticity are induced.[40]

In systems with multiple feedback interactions at differing timescales, understanding response dynamics to simple perturbations can reveal how the constitutive mechanisms interact and
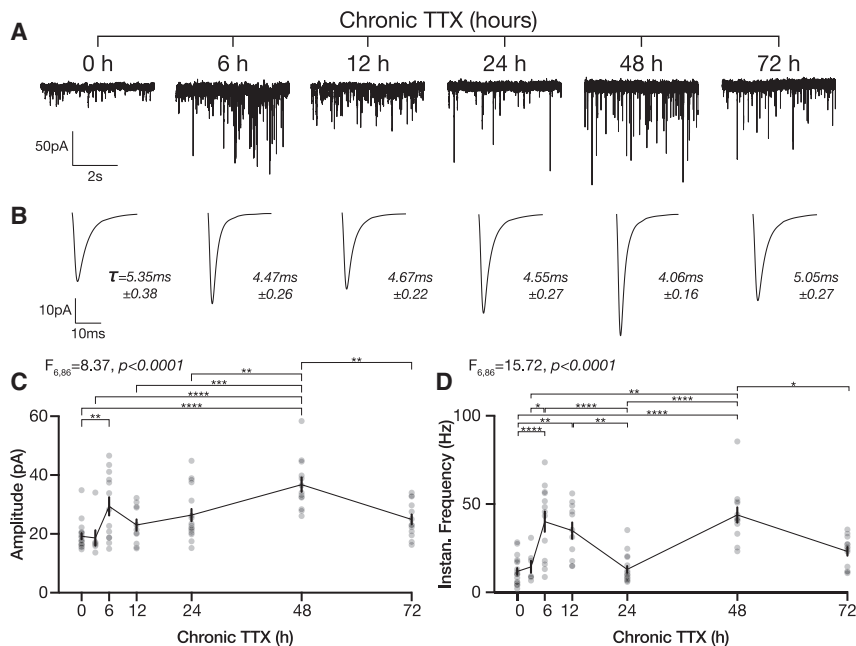
Figure 1. Homeostatic upscaling of synaptic weight exhibits slow non-monotonic changes in mEPSC properties

(A) Example voltage-clamp recordings of neurons chronically treated with TTX for 0, 6, 12, 24, 48, and 72 h.

(B) Mean mEPSC waveforms of the mean waveforms and mean decay τ of neurons recorded from corresponding TTX time points in (A).

(C) Mean ± SEM amplitude of mEPSCs, individual cells as gray circles.

(D) Mean ± SEM frequency of mEPSCs. Throughout, symbols signifying corrected multiple comparison, with *p < 0.05, **p < 0.01, ***p < 0.001, ****p < 0.0001, detailed in supplemental tables. Statistical testing: 1-way ANOVA (Table S2). See also Figures S1–S3.

RESULTS

Adaptation to inactivity is a slow non-monotonic response

To delineate the time course of inactivity-induced synaptic homeostasis, we recorded miniature excitatory postsynaptic currents (mEPSCs, or minis) from neuronal cortical cultures chronically treated with TTX for 0, 3, 6, 12, 24, 48, and 72 h (±1.5 h) between 13 and 17 days *in vitro* (DIV) and characterized changes in mEPSC amplitude, frequency, and kinetics. Based on previous reports, we expected that the average amplitudes of mEPSCs would increase after 3 h of TTX,[38] rise monotonically,[53,54] and persist until 72 h.[55] To the contrary, the increase in mEPSC amplitude was strikingly non-monotonic, with observed peaks at 6 and 48 h of TTX treatment (Figures 1C and S1C). mEPSC instantaneous frequency also displayed a significant non-monotonic, seemingly oscillatory change with TTX treatment (Figures 1D and S1D). In addition to the predicted amplitude increase, mEPSCs from TTX-treated neurons displayed a broad decrease in decay constants (decay τ) (Figures S1A and S1B). These data show that upscaling of excitatory synapses during prolonged spike blockade is not monotonic but instead appears to oscillate.

L-type Ca²⁺ channel voltage activation shapes the time course of the homeostatic response

Although voltage-gated Ca^{2+} channels have been implicated in synaptic strength regulation for over a decade,[28] their precise role in inactivity-induced homeostasis remains a mystery. We used a mouse model of the TiS (TS2-neo) gain-of-function mutation G406R[56] to investigate what aspects of LTCC signaling could be involved in homeostasis and how these aspects may contribute to the dynamic changes we observed. TiS is a syndromic form of autism[57] that arises from a point mutation in the $Ca_V1.2$ Ca^{2+} channel. This mutation causes a shift in the voltage-activation curve and impaired inactivation of Cav1.2, resulting in channel openings from smaller depolarizations with increased Ca^{2+} flux when compared to wild-type (WT) $Ca_V1.2$.[51,52,58] This mutation also leads to exaggerated voltage-dependent conformational signaling

provide valuable insights into the behavior of the system in complex biologically relevant contexts.[41] Theoretical studies generally model homeostatic synaptic plasticity as a control system[42,43] wherein kinetic differences of positive or negative feedback components determine response dynamics, which can be monotonic, oscillatory, or unstable.[44–47] Despite theoretical emphasis on the temporal properties of homeostatic adaptations, experimental studies often center on one or two recorded time points after a perturbation in firing rate or synaptic transmission.[10,28,48,49] No study so far has linked response dynamics and its mechanisms following a simple, stepwise intervention in neuronal activity. Understanding these dynamics could reveal a functional organization of the diverse molecular players used by homeostatic and Hebbian plasticity.

Here, we show that the response to a widely used homeostatic perturbation, activity silencing by tetrodotoxin (TTX), is a non-monotonic, near-oscillatory fluctuation involving transient increases of CPARs. These hitherto-overlooked dynamics require an ordered sequence of CaN deactivation[10] and CaMKII recruitment and activation.[50] We also found that LTCCs tune these dynamics by studying responses in neurons harboring a $Ca_V1.2$ mutation associated with Timothy syndrome (TiS), a rare but highly penetrant form of autism.[51,52] Building on these experimental observations and manipulations, we propose a quantitative model of synaptic homeostasis that incorporates dynamic interactions between positive and negative feedback signaling. Our findings support the premise that synaptic responsiveness is a variable under feedback control and that spine Ca^{2+}/CaM acts as the sensor to recruit "Hebbian" and "homeostatic" elements to stabilize synapses and prepare them for future input. Intriguingly, both our experiments and model provide mechanistic links between synaptic Ca^{2+} homeostasis and activity-dependent regulation of spike width, showing how decentralized synapses could subsequently regulate cell-wide properties.
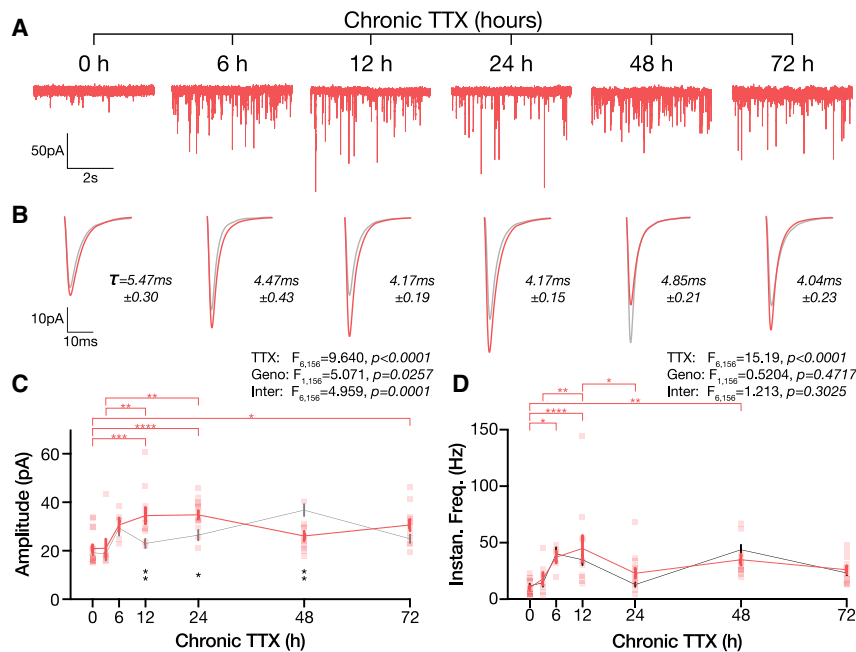
Figure 2. Neurons with the TiS Cav1.2 gain-of-function mutation possess an altered homeostatic time course

(A) Example voltage-clamp recordings of TiS neurons chronically treated with TTX for 0, 6, 12, 24, 48, and 72 h.

(B) Mean mEPSC waveforms of the mean waveforms of neurons recorded in the corresponding TTX time point in (A). WT waveforms from Figure 1 in gray.

(C) Mean ± SEM amplitude of mEPSCs from TiS (red, individual cells as red squares) and WT (gray from Figure 1).

(D) Mean ± SEM frequency of mEPSCs from TiS (red) and WT (gray). Red stars indicate corrected significant differences in TiS TTX-treated time points. Black stars indicate corrected significant differences between WT and TiS at time point. Statistical testing: 2-way ANOVA (Table S3). See also Figures S2 and S3.

GluA1-containing CPARs support synaptic homeostasis at time points of peak mEPSC amplitude and fastest decay

(VΔC) and kinase activity during excitation, and contributes to the homeostatic elevation of spontaneous synaptic Ca^{2+} transients.[15,48] We hypothesized that the TiS mutation would affect the overall magnitude of synaptic homeostasis.

Surprisingly, mEPSCs from litter-matched-TiS cultures exhibited similarly non-monotonic upscaling, as seen in their WT counterparts, but with differing phases in the oscillatory-like changes in amplitudes. Time points of peak amplitude in TiS significantly differed from WT at time points of 12, 24, and 48 h (Figures 2C and S2C). Within TiS groups, there was a significant change in amplitude at 12, 24, and 72 h of TTX (Figures 2C and S2C) and in frequency at 6, 12, 24, and 48h of TTX (Figures 2D and S2D). We did not observe a phase alteration of mEPSC frequency (Figures 2D and S2D) or for mEPSC decay time constants (Figures S2A and S2B) between WT and TiS. These results indicate that the voltage activation of Ca$_V$1.2 alters the dynamics, not the magnitude, of excitatory synaptic homeostasis.

mEPSC properties do not developmentally fluctuate

To confirm that our observations were not confounded by developmental or non-homeostatic changes, we recorded mEPSCs from cultures at DIV during which all TTX experiments were conducted (Figure S3). We did not observe significant changes in mEPSC amplitude or frequency 13–17 DIV (Figures S3C and S3E) in either WT or TiS cultures. We observed a small increase in decay kinetics through DIV (Figures S3G and S3J). These changes did not fluctuate, in contrast to the changes in mEPSC kinetics seen with homeostatic perturbations, all suggesting that any *in vitro* developmental changes in synaptic and network properties did not confound our measurements and observations of adaptation to activity perturbation.
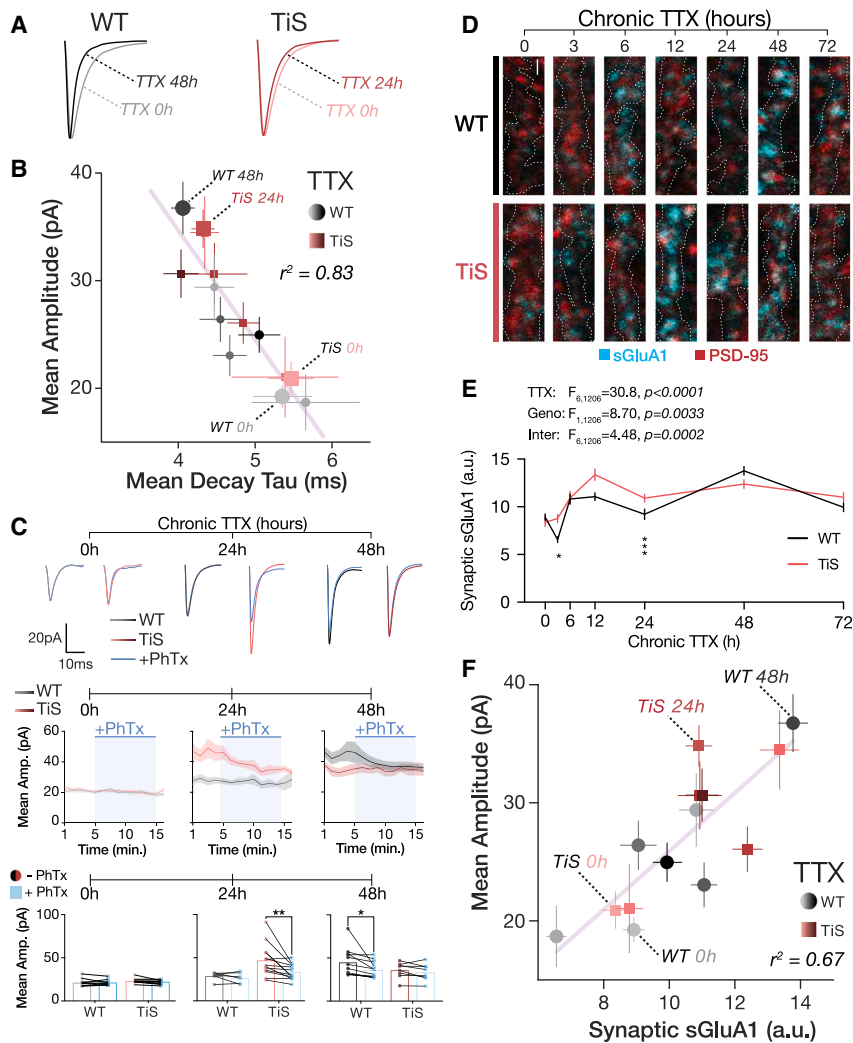
To determine whether LTP-associated CPARs contribute to the dynamic homeostatic response, we first compared the mean mEPSC waveforms at various time points from our TTX experiments in both WT and TiS (Figures 1 and 2) and found that mEPSCs with higher amplitudes consistently exhibited faster decays (Figure 3A). Plotting the mean amplitude (ordinate) against the mean decay τ (abscissa) for each time point revealed a strong negative correlation (Figure 3B). Changes in mEPSC decay time reflects AMPAR composition and the prevalence of GluA1 relative to GluA2. mEPSC events with fast decay times point to a prevalence of CPARs.[59] We confirmed that at time points of highest amplitude and fastest decay, mEPSCs were CPAR dominated. We verified this by recording from 0, 24, and 48 h TTX-treated cultures while acutely exposing them to philanthotoxin (PhTx), a CPAR-specific antagonist. mEPSCs only exhibited PhTx sensitivity at specific hours of chronic TTX treatment. WT cultures treated with TTX for 48 h displayed a PhTx-induced reduction in mEPSC amplitude (Figure 3C, bottom right) and increase in decay τ (Figure S4F). TiS cultures were not PhTx sensitive at 48 h but were responsive earlier at 24 h instead (Figures 3C, center, and S4F). We noted that mEPSCs from TiS cultures at baseline exhibited slight sensitivity to PhTx, as indicated by an increase in decay τ (Figure S4F). Although WT neurons exhibited a significant decrease in mEPSC frequency at 24 h TTX + PhTx (Figure S4G), TiS neurons displayed no notable PhTx-induced frequency changes at any time point tested (Figures S4E and S4G).

We then assessed whether there were changes in GluA1 levels during prolonged inactivity by measuring levels of surface GluA1 (sGluA1) with immunofluorescence. We colabeled sGluA1 and postsynaptic density protein 95 (PSD-95) in cultures and measured the mean intensities of the sGluA1 signal within PSD-95 puncta in dendritic regions identified by microtubule-associated protein 2 (MAP2) immunolabeling (Figure 3D, white

Figure 3. Ca²⁺-permeable GluA1-containing AMPARs transiently contribute to high-amplitude time points of synaptic homeostasis

(A) Scaled mean mEPSC waveforms from Figures 1 and 2 for WT (48 h TTX, black) and TiS (24 h TTX, red) compared to 0 h TTX.

(B) Mean ± SEM amplitude vs. the mean ± SEM decay of all time points (0–72 h TTX, light to dark) and genotypes (WT gray to black, TiS pink to maroon).

(C) Top: Mean mEPSC waveforms from voltage-clamp recordings with the corresponding TTX time point before PhTx wash-on (WT gray to black; TiS pink to maroon) and after PhTx wash-on in blue. Center: Time course of mean ± SEM mEPSC amplitudes with PhTx wash-on in blue. Bottom: Matched amplitude means from 3 min of baseline preceding PhTx wash-on and last 3 min of PhTx recording.

(D) Representative micrographs of sGluA1 (cyan) and PSD-95 (red) from cortical cultures chronically treated with TTX. Dendritic region of interest (ROI) was determined by MAP2 staining, represented as white dotted line outline. Scale bar, 1 μm.

(E) Time course of mean ± SEM sGluA1 intensities within PSD-95 puncta of a dendritic ROI from (D).

(F) Mean ± SEM amplitude vs. mean ± SEM synaptic sGluA1 for time points (0–72 h TTX, light to dark) and genotypes. Statistical testing: linear regression, 2-way ANOVA (Tables S4 and S5). See also Figure S4.

outline). We observed a non-monotonic increase in synaptically localized sGluA1 in both WT and TiS cultures, with significant differences between WT and TiS at 3 and 12 h of chronic TTX (Figure 3E). Broadly, TTX treatment increased the intensity of sGluA1 puncta, with the highest intensity at time points predictable from our electrophysiological data (Figure 3F). We also saw similar changes in shaft sGluA1 (Figures S4J and S4K), suggesting that synaptic increases were not accounted for by the relocation of GluA1. These results indicate that the composition of upscaled synapses changes over the course of homeostatic adaptation by transiently incorporating the GluA1 AMPAR subunit, typically associated with LTP.[20] Taken together, our results show that the dynamic inclusion of GluA1-containing CPARs contributes to increasing synaptic weight in response to prolonged inactivity.

Chronic CaN blockade mimics early synaptic homeostasis with a monotonic time course

The multiphasic response suggests that two opposing signaling pathways interact during prolonged inactivity. We hypothesized

that peaks in mEPSC amplitudes may involve variations in local Ca²⁺ signaling involving Ca$_V$1.2 (Figure 2) and GluA1/CPARs (Figure 3). A corollary of this hypothesis is that the initial reduction of activity would alter a participatory Ca²⁺-signaling enzyme. The Ca²⁺/CaM-dependent phosphatase CaN, previously implicated in both rapid and prolonged synaptic homeostasis through the action of CPARs,[9,10,25] was a promising candidate. We predicted that TTX results in a reduction of CaN activity, via Ca²⁺ signaling through Ca$_V$1.2, to mediate early synaptic upscaling. To determine the time course of the involvement of CaN, we chronically blocked CaN in WT and TiS cultures with FK506, an inhibitor of CaN activity. In both genotypes, we observed a broad increase in mEPSC amplitudes by 6 h of chronic FK506 (5 μM) that persisted through 12 h and 24 h (Figures 4C, S5A, and S5G). TiS cultures exhibited a quicker and larger increase in mEPSC amplitudes compared to WT, as indicated by different exponential constants (Figure 4C, dashed lines). These amplitude changes paralleled drops in decay time constants (Figures 4D, S5C, and S5I) and increases in frequency (Figures 4E and S5E–S5K). Interestingly, chronic CaN inhibition in WT cultures did not evoke a drop in mEPSC amplitudes after 6 h, as seen in TTX-treated conditions (Figure 4F), whereas kinetic properties of the mEPSCs remained comparable (Figure 4G), implying that CaN may be reactivated after an initial response in TTX-induced upscaling.
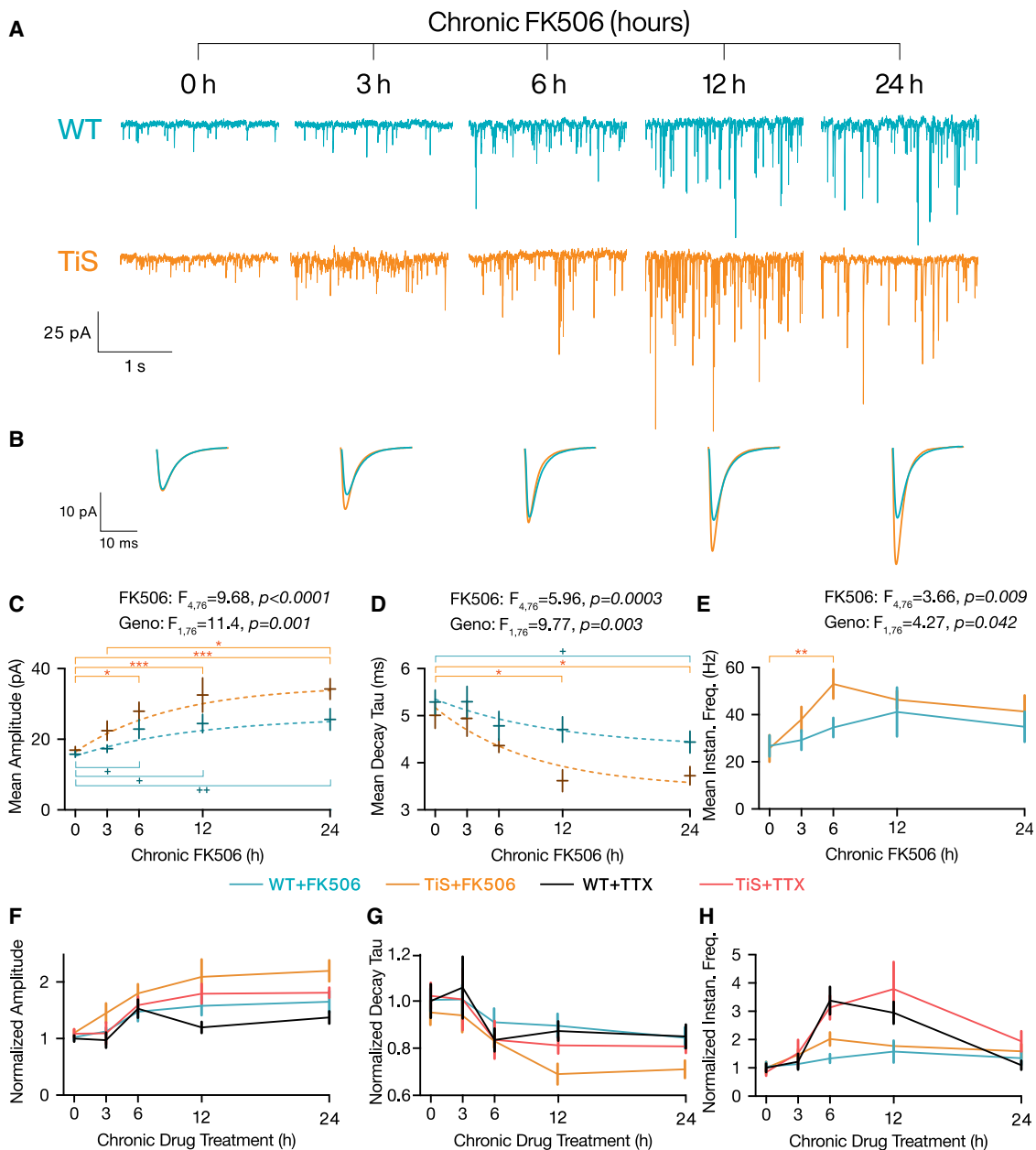
Figure 4. Chronic inactivation of CaN elicits monotonic synaptic upscaling

(A) Example voltage-clamp recordings of WT (teal) and TiS (orange) neurons chronically treated with CaN inhibitor FK506 for 0, 3, 6, 12, and 24 h.

(B) Mean mEPSC waveforms of neurons recorded in the corresponding FK506 time point.

(C) Mean ± SEM (solid crosses) amplitude of mEPSCs from FK506-treated neurons WT (teal) and TiS (orange) with exponential fit (dotted line, time constants are WT τ_{FK}: 11.4 h, TiS τ_{FK}: 9.3 h).

(D) Mean ± SEM (solid crosses) decay kinetics of mEPSCs from FK506-treated neurons, with exponential fit (dotted line, time constant τ_{FK}: 11.4 h, rate constant of 1.46×10^{-3} min^{-1}). This rate provided a constraint on the parameters of a computational model (Figure 7), as detailed in Table S1.

(E) Mean ± SEM instantaneous frequencies of mEPSCs from FK506-treated neurons.

(F) Normalized mean ± SEM amplitude of mEPSCs from neurons: WT-TTX (black), TiS-TTX (red), WT-FK506 (teal), and TiS-FK506 (orange) over first 24 h of drug treatment.

(G) Normalized mean ± SEM decay tau of mEPSCs over first 24 h of drug treatment.

(H) Normalized mean ± SEM instantaneous frequency of mEPSCs over first 24 h of drug treatment. Statistical testing: 2-way ANOVA, + signifies post hoc Fisher's least significant difference (Table S6). See also Figure S5.
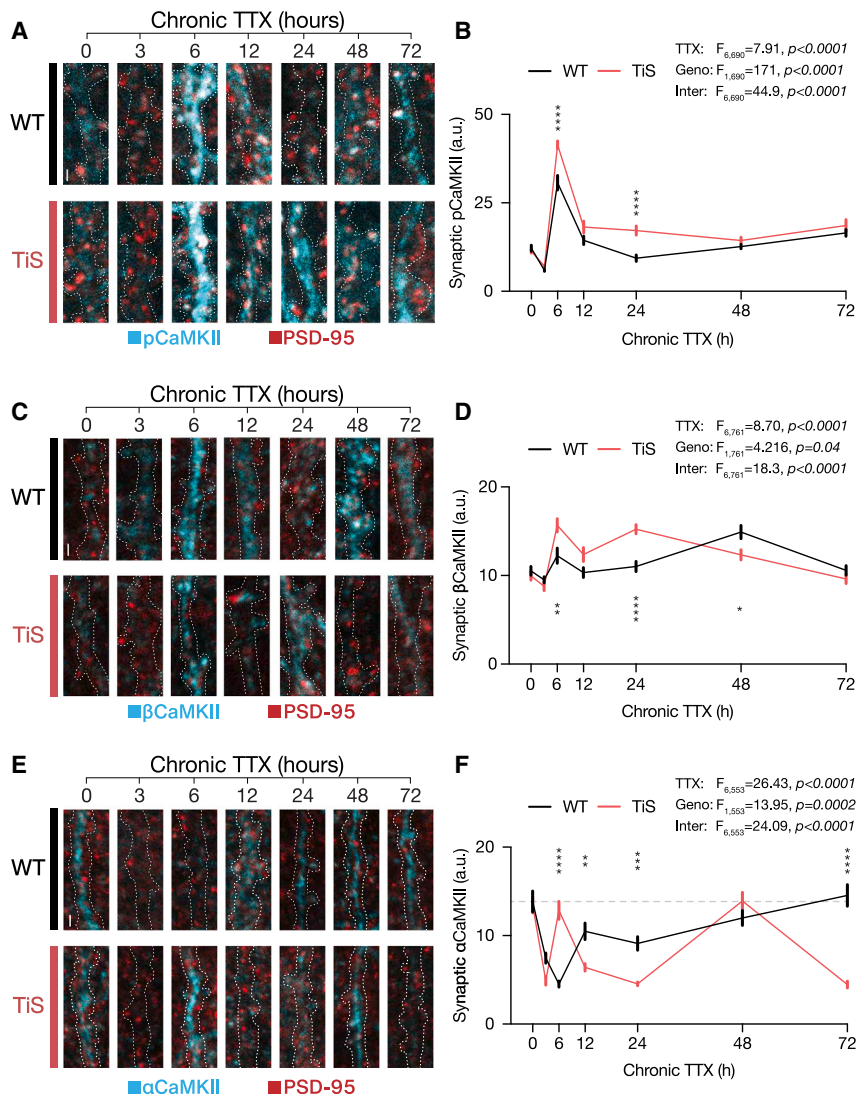
Figure 5. CaMKII activation and isoform expression fluctuates through TTX-induced homeostasis

(A) Representative micrographs of pCaMKII (cyan) and PSD-95 (red) from cortical cultures chronically treated with TTX. Dendritic ROI was determined by MAP2 staining, represented as white dotted line outline.

(B) Time course of mean ± SEM pCaMKII intensities within PSD-95 puncta from (A).

(C) Representative micrographs of βCaMKII (cyan) and PSD-95 (red) from cortical cultures chronically treated with TTX. Dendritic ROI was determined by MAP2 staining, represented as white dotted line outline.

(D) Time course of mean ± SEM βCaMKII intensities within PSD-95 puncta from (C).

(E) Representative micrographs of αCaMKII (cyan) and PSD-95 (red) from cortical cultures chronically treated with TTX. Dendritic ROI was determined by MAP2 staining, represented as white dotted line outline.

(F) Time course of mean ± SEM αCaMKII intensities within PSD-95 puncta from (E). Scale bars, 1 μm. Statistical testing: 2-way ANOVA (Table S7). See also Figures S6 and S7.

and S7A). At other time points when pCaM-KII was less active, we still observed smaller but significant differences in its amount of activation over time. These dynamic changes were observed at both putative synapses (within PSD-95 puncta; Figures 5B, S6A, and S6C) and putative dendritic shafts (not in PSD-95 puncta; Figures S6B, S6D, and S7A). These results extend previous observations on synaptic inactivity and provide a dynamic picture of CaMKII regulation in response to spike blockade.
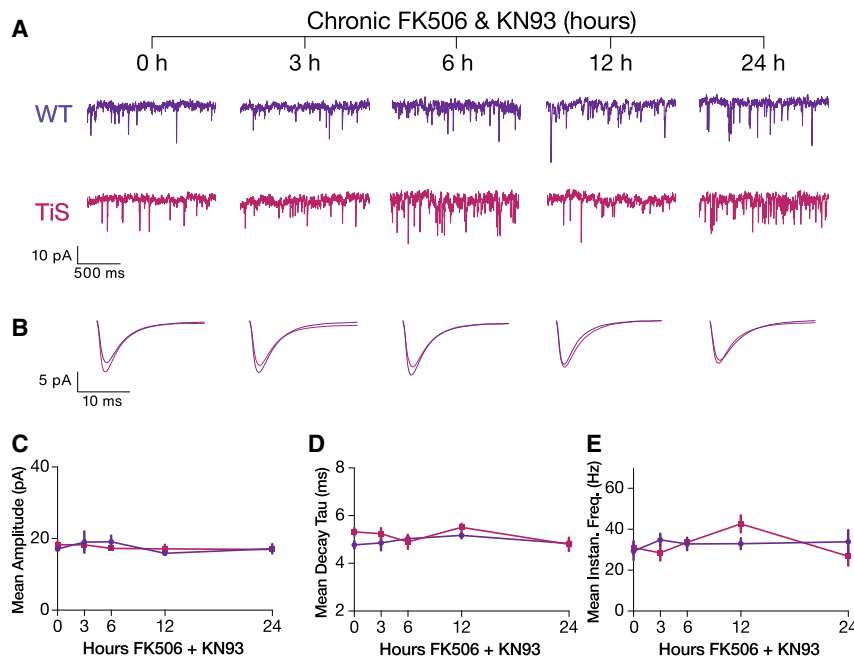
Transient increase in CaMKII phosphorylation during adaptation to chronic inactivity

We next hypothesized that the upregulation of GluA1 in either TTX- or FK506-treated neurons is driven by another Ca^{2+}-dependent enzyme, CaMKII. Furthermore, the monotonic synaptic upscaling from FK506 treatment suggests that the TTX-induced multiphasic response may result from concerted, but not simultaneous, CaN inactivity and CaMKII activity. Since the formation of phosphorylated CaMKII (pCaMKII) is one avenue to CaMKII activation, we colabeled T286/287-pCaMKII and PSD-95 in TTX-treated cultures in dendritic regions identified by MAP2 immunolabeling. TTX treatment led to dynamic changes in pCaMKII levels in both WT and TiS (Figures 5A, 5B, S6, and S7). We discovered a strong transient activation of CaMKII at 6 h of chronic TTX treatment that decreased to an above-baseline level at 12 h of TTX in both WT and TiS cultures. In contrast to other TiS results, the magnitude of pCaMKII at 6 and 24 h of TTX in TiS neurons was significantly greater than that of WT (Figures 5B, S6A–S6D,

Synaptic levels of both β and α isoforms of CaMKII fluctuate in response to inactivity

We previously demonstrated that prolonged spike blockade shifts the predominant CaMKII isoforms from α to β.[50] Because the βCaMKII holoenzyme is ~8-fold more sensitive to Ca^{2+}/CaM,[60] increased β/α could mediate the homeostatic regulation of CaMKII activity. To understand how both βCaMKII and αCaMKII changed over time during TTX-induced homeostasis of excitatory synapses, we colabeled specific CaMKII isoforms with PSD-95 in separate cultures and measured the intensities of the CaMKII signal within PSD-95 puncta in dendritic regions identified by MAP2 immunolabeling.

For synaptic βCaMKII levels, we found a general increase after 6 h of chronic TTX treatment (Figures 5C, 5D, and S6E–S6H), with similar non-monotonic changes in βCaMKII levels in the dendritic shaft (Figure S7B). These increases differed between WT and TiS (Figures 5C and 5D). βCaMKII levels seemingly oscillate in WT neurons, with elevations of synaptic βCaMKII mirroring

A
Chronic FK506 & KN93 (hours)

0 h   3 h   6 h   12 h   24 h

WT

TiS

10 pA |
500 ms

B

5 pA |
10 ms

Figure 6. CaMKII blockade prevents FK506-induced upscaling

(A) Mean mEPSC waveforms from neurons of corresponding FK506+KN93 time point.

(B) Mean mEPSC waveforms of the mean waveforms of neurons recorded in the corresponding FK506+KN93 time point. WT (purple), TiS (magenta).

(C) Mean ± SEM amplitude kinetics of mEPSCs from FK506+KN93-treated neurons. WT (purple), TiS (magenta).

(D) Mean ± SEM instantaneous frequencies of mEPSCs from FK506+KN93-treated neurons.

(E) Mean ± SEM decay kinetics of mEPSCs from FK506+KN93-treated neurons. Statistical testing: 2-way ANOVA (Table S8). See also Figure S8.

C Mean Amplitude (pA) — Hours FK506 + KN93

D Mean Decay Tau (ms) — Hours FK506 + KN93

E Mean Instan. Freq. (Hz) — Hours FK506 + KN93

that of mEPSC amplitude, peaking at 6 and 48 h of TTX treatment (Figures 5C and 5D). In TiS neurons, synaptic levels of βCaMKII quickly rose by 6 h of TTX, followed by a slight fluctuation before returning to baseline levels at 72 h. Notably, in WT the mean mEPSC amplitude was linearly correlated with the βCaMKII level at the same time point (Figure S7D, r^2 = 0.8975); the correlation was weaker in TiS cultures (Figure S7E, r^2 = 0.4512). The increase in βCaMKII and the transient activation of CaMKII suggest that LTP mechanisms are used in low-activity scenarios through an increased availability of the βCaMKII isoform.

For αCaMKII, we observed broad non-monotonic decreases in synaptic and dendritic shaft levels in response to TTX, with significant differences between WT and TiS (Figures 5E, 5F, S6I–S6L, and S7C). αCaMKII levels in WT significantly dropped after 3 h of TTX, reaching a nadir by 6 h, before recovering at 72 h (Figure 5F). In contrast, αCaMKII levels in TiS neurons oscillated, with significant troughs at 3, 24, and 72 h of TTX treatment (Figure 5F). Between WT and TiS, αCaMKII levels differed at 6, 12, 24, and 72 h, suggesting that the dynamics of αCaMKII isoform expression in response to inactivity were affected by the Ca$_V$1.2 mutation. Our data confirm that α- and βCaMKII levels change in opposite directions in response to inactivity.[50] Increases in βCaMKII occur with slow multihour kinetics, consistent with a series of steps such as activation of transcription, translation, and intermediate steps of mRNA/protein transport.[61]

Blockade of CaMKII prevents FK506-induced upscaling

Our results suggest that the cooperation between CaN and CaMKII may be necessary to upscale excitatory synapses early in response to prolonged activity reduction. To experimentally confirm whether CaMKII activity was necessary for this early response, we cotreated WT and TiS cultures with FK506 and KN93 to pharmacologically block CaMKII activation and

measured mEPSCs at 0, 3, 6, 12, and 24 h. When the efficacies of CaN and CaMKII were simultaneously reduced, we saw no change in mEPSCs. mEPSC amplitudes in both WT and TiS did not increase over a 24-h period (Figures 6A–6C and S8A–S8D). mEPSC decay kinetics did not change significantly (Figures 6D and S8E–S8H), nor did instantaneous frequencies of mEPSCs (Figures 6E and S8I–S8L). These results suggest that synaptic upscaling due to deactivation of CaN requires activity of CaMKII.

Integrating negative and positive feedback via phosphatase and kinase actions captures key features of homeostatic response

Our results indicate that TTX-induced inactivity leads to dynamic changes in mEPSC properties (Figures 1 and 2) and demonstrate the necessity of CaMKII and CaN activity (Figures 4, 5, and 6). To determine whether the interaction of these signaling pathways is sufficient to produce a multiphasic homeostatic response, we used a reduced model of Ca^{2+}-dependent phosphorylation of GluA1 (Figure 7, see model supplement). In the model, postsynaptic Ca^{2+} is determined by the presynaptic quantal rate, R, via the equation

$$\log Ca = Ca_0 + Ca_{PSP0}R + \overline{Ca}_{GluA1}RA,$$

where $\log Ca$ is the log concentration of postsynaptic Ca^{2+} available to be bound to CaM; in linear units, Ca_0 is a baseline level of Ca^{2+}, $\overline{Ca}_{GluA1}$ is the maximal Ca^{2+} per quantal rate through CPARs, and Ca_{PSP0} is the Ca^{2+} per quantal rate through CPAR-independent sources. The postsynaptically functional fraction of CPARs, A, is determined by a kinetic equation

$$\frac{dA}{dt} = k_f(1 - A) - k_d A,$$

in which k_f and k_d represent the rate of GluA1 phosphorylation and dephosphorylation. The phosphorylation rates (k_f, k_d) (Equation S1) depend on activation variables m and n, which represent the activation of CaMKII and CaN, respectively, and b, which represents the proportion of CaMKII that is βCaMKII
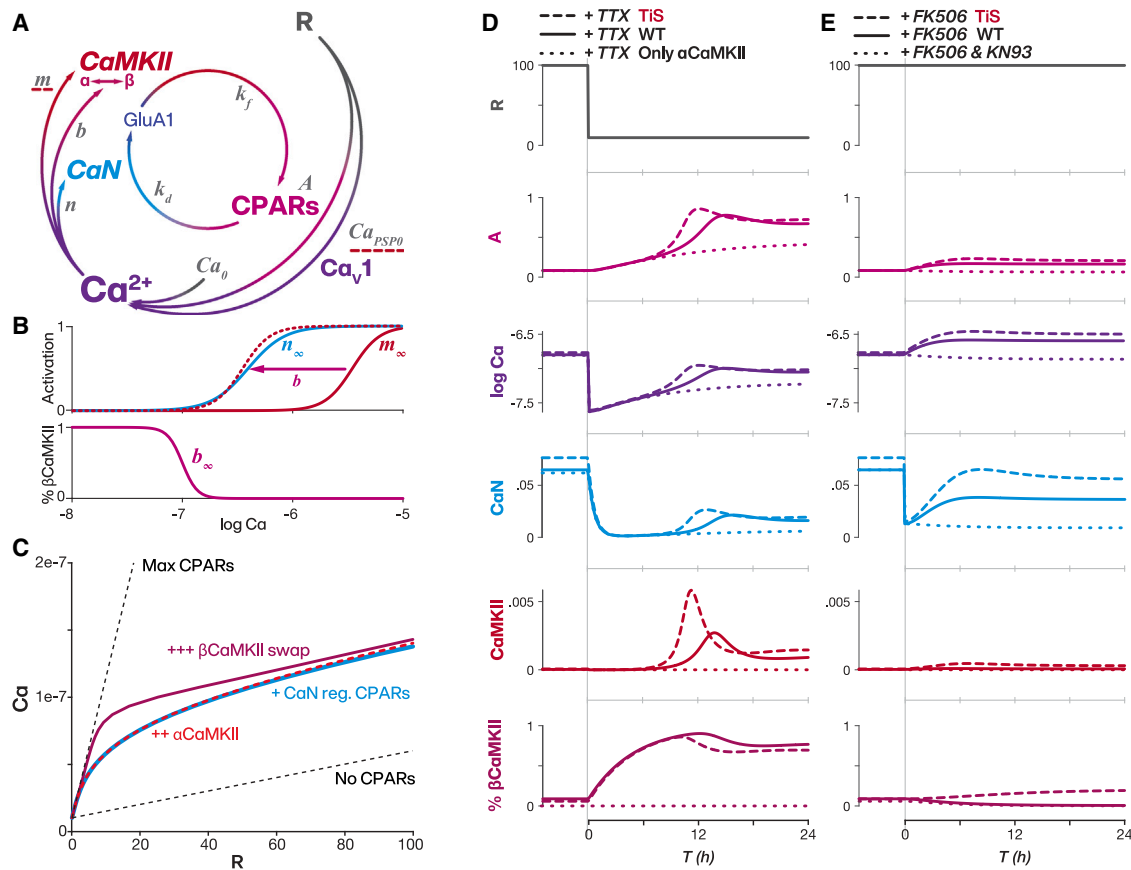
Figure 7. Integrating Ca²⁺-dependent phosphorylation feedback captures key features of homeostatic response

(A) Schematic of signaling players (colors) with related mathematical variables (gray). Variables modified to model TiS G406R mutation with red dashed underline.

(B) Activation curves of n (CaN, blue), m (100% αCaMKII solid red, 100% βCaMKII dotted red), and in bottom b, signifying CaMKII ratio $b = \beta/(\alpha + \beta)$, (%βCaMKII). Subscript ∞ denotes steady-state value.

(C) $Ca(R)$ curve, the steady-state level of Ca²⁺ as a function of quantal rate (R). Full range of steady states exhibited by the model $A = 0$ and $A = 1$ (black dotted lines). For the cases of CaN-homeostasis only ($k_{CaMKII} = 0$, light blue), for CaN-homeostasis with αCaMKII only ($Ca_{\Delta b} = 0$, red dotted line), and the full model with switchover from αCaMKII to βCaMKII (maroon line).

(D) Model response to the TTX manipulation without presynaptic oscillation by clamping presynaptic quantal release from a baseline level of 100 Hz to "TTX" level of 10 Hz with WT (solid lines), TiS (dashed line), and without α- to βCaMKII switch (dotted line) for GluA1 (magenta line), log Ca (purple line), CaN (blue line), CaMKII (red line), and %βCaMKII (maroon line).

(E) Model FK506 with WT parameter (solid lines) and TiS parameter (dashed lines) responses to CaN inhibition simulated by reducing CaN efficacy to 20% while maintaining quantal rate ($R = 100\ Hz$). Predicted model response to FK506 and KN93 (dotted lines) by reducing CaN and CaMKII efficacy while maintaining quantal rate. See also Figures S9 and S10 and model supplement.

and thus determines the Ca²⁺ sensitivity of CaMKII. In turn, m, n, and b are determined by the level of Ca²⁺ and follow first-order kinetics with exponential time constants of 1, 40, and 300 min, respectively. The model is thus composed of four dynamical variables that represent the activity of CaN, CaMKII, and CPARs, their relationship with postsynaptic Ca²⁺, and the influence of presynaptic rate (Figure 7B; see model supplement and Table S1 for further interpretation of model equations, parameters, and variables).

To understand the relative contribution of the various phosphokinetic components, we first considered their effect on the steady-state response of the model as a function of quantal rate (Figure 7C). Without CPARs ($A = 0$), Ca²⁺ increases linearly with R, reflecting Ca_{PSP0}. When the proportion of functional CPARs is clamped at $A = 1$, the slope of this relationship in-

creases dramatically. If A is allowed to vary according to the phosphatase activity of CaN, then the operating curve (light blue) swings between the extremes delineated by fully functional and non-functional CPARs. This highlights the impact of Ca²⁺/CaM regulation of CaN, which buffers the dependence on rate by adjusting CPAR-mediated Ca²⁺ entry per quantum. Incorporation of the influence of αCaMKII (dashed red line) has little effect on the operating relationship because CaMKII is negligibly recruited at near-basal Ca²⁺ levels, whereas at the high quantal rate, αCaMKII activation results in bistability between a high-[Ca²⁺] CaMKII-active and low-[Ca²⁺] CaMKII-inactive state (Figures S9A and S9B). In contrast, the Ca²⁺-dependent replacement of αCaMKII with βCaMKII significantly affects basal Ca²⁺ (Figures 7C and S9A), boosting the steady-state Ca²⁺ curve at low rates and flattening it further. In combining the negative

feedback effects of CaN deactivation and βCaMKII, this steady-state relationship allows [Ca^{2+}] to increase by only ∼40%, with a 5-fold variation in quantal rate (e.g., between 20 and 100 Hz).

To understand the dynamic changes in [Ca^{2+}] and glutamate receptor level following spike blockade, we turned next to modeling time-dependent changes in log Ca and A that follow a sudden change in R (Figure 7D). To mimic the application of TTX, we reduced R from a "baseline" rate of 100 Hz that incorporates quantal release due to spontaneous action potential firing, to a "TTX" quantal rate of 10 Hz, comparable to our data (Figure S9A). The sharp decrease in rate caused a rapid shift in log Ca from −6.9 to −7.6, and a corresponding decrease in CaN activity. This in turn leads to a slow increase in GluA1, driven by the basal level of protein kinase activity that brings log Ca back toward steady-state levels. Simultaneously, the altered log Ca caused an increase in βCaMKII, which eventually shifted the Ca^{2+} sensitivity of CaMKII enough to trigger a rapid activation of CaMKII and recruitment of CPAR at ∼8 h; this in turn leads log Ca to return near its pre-TTX steady-state level. Thus, the interaction of CaN and CaMKII and the transition between α- and βCaMKII isoforms is sufficient to account for the first peak in mEPSC amplitude (Figure 1) and the corresponding large peak in synaptic pCaMKII (Figure 5A). This simulates the data observed following 24 h of TTX. To model the effects of the TiS mutation, CPAR-independent Ca^{2+} permeability and effective Ca^{2+} sensitivity of CaMKII were increased (Figure 7A, dashed red underline), mimicking the effect of prolonged LTCC currents[51,58] and heightened relocation of CaMKII to dendritic spines.[15] This resulted in exaggerated CaMKII activation and GluA1 levels (Figure 7D, dashed lines). However, these dynamic features were abrogated if b was held fixed at 0 (Figure 7D, dotted lines), highlighting the contribution of the α- to βCaMKII conversion.

We also simulated the synaptic response to FK506 application by inhibiting CaN-mediated dephosphorylation by clamping R at its baseline rate, and at $t = 0$, reduced CaN efficacy to a small fraction of its basal value. In response, the basal level of protein kinase activity k_{f0} drove A to a new, higher steady state with first-order kinetics (Figure 7E, solid line), in line with the monotonic change in quantal amplitude upon exposure to FK506 (Figure 5). In contrast, when we simultaneously reduced CaN activity and CaMKII efficacy as well, the slow increase in A was not seen (Figure 7E, dotted line). In addition, with a TiS mutation-like modification of the model, A rose more quickly to a higher steady state in response to FK506 (Figure 7E, dashed line). We also investigated model responses to stepwise quantal release decreases of varying degrees (Figure S9D, 100 Hz to 90, 70, 40, and 10 Hz, light to dark gray). Smaller decreases in quantal release exhibited faster and smaller responses in A that qualitatively appeared monotonic (Figure S9D, light magenta lines), with the non-monotonic response appearing only with large stepwise decreases in quantal release (dark magenta lines).

We noted that the model did not produce the secondary peak in GluA1 at ∼48 h of TTX (Figure 1C). We hypothesized that the longer-timescale phase in mEPSC amplitude and CPARs changes may be a result of fluctuations in presynaptic spontaneous release,[36] suggested by fluctuations in mEPSC frequency in our data (Figure 1D). To test for this possibility, we imposed a

damped oscillation in R mimicking the observed mEPSC frequency changes (Figures 1D and S9C, top; see model supplement). This robustly produced a late peak in GluA1 (Figure S9C, gray shading), with a larger and earlier CaMKII peak (6 h) in the first cycle (Figure S9C, red shading) reproducing experimental observations (Figures 1 and 5). Taken together with the simulation without a presynaptic oscillation (Figure 7D), this model response highlighted three stages of the adaptation to prolonged reduction in activity. First, a rapid drop in Ca^{2+} results in the inactivation of CaN, allowing GluA1 phosphorylation to rise due to the basal activity of protein kinases, including CaMKII (Figure S9C, blue shading). Second, if the rate remains sufficiently low for a long period, then a large and transient peak in CaMKII phosphorylation activity occurs at ∼6–12 h, mediated by a slow increase in the β/α ratio (Figure S9C, red shading). The third stage (Figure S9C, gray shading) is dominated by the slow presynaptic oscillation in R. Notably, inclusion of the presynaptic oscillation brought postsynaptic Ca^{2+} levels closer to the pre-TTX condition than without any presynaptic oscillation. Taken together, these simulations of Ca^{2+}-sensitive phosphatase and kinase activities, respectively providing negative and positive feedback, mimicked the dynamics of inactivity-dependent synaptic plasticity.

DISCUSSION

Homeostatic synaptic plasticity is classically pictured as a slow process that readjusts synaptic weights to stabilize circuit activity despite Hebbian plasticity. Our results indicate that the multiphasic response to spike blockade (Figures 1, 2, and 3) arises from sequential changes in Ca^{2+}-dependent phosphatase and kinase activities (Figures 4, 5, 6, and 7). First, inactivity causes a rapid drop in Ca^{2+}, leading to the deactivation of CaN (Figure 4) and increases in phosphorylated GluA1 due to baseline kinase activity, paralleled by a switchover from α- to βCaMKII expression (Figures 5C, 5D, 7D, and S9C). Second, βCaMKII-mediated kinase activity peaks at ∼6–12 h (Figures 7D, S9C, 5A and 5B). Finally, a slow oscillation in quantal rate ensues. Our experiments verified the necessity of CaMKII for generating the fluctuating response (Figure 5) and coordination between CaN and CaMKII in generating even the earliest postsynaptic strengthening (Figure 6).

Excitatory synapses engage Hebbian mechanisms to homeostatically regulate Ca^{2+} and preserve synaptic responsiveness

We found that elements of LTP (CaMKII) are transiently engaged during homeostatic plasticity, albeit more slowly than in LTP, and interact with more canonical homeostatic elements.[10,25,62–64] CaMKII is essential for synapse strengthening in LTP,[65] which is induced by brief but intense neuronal activity.[66] Thus, it seems paradoxical that CaMKII is activated by prolonged inactivity.[38,64,67] However, the elimination of action potentials tilts the balance of CaMKII isoforms from αCaMKII to βCaMKII,[50] increasing Ca^{2+}/CaM sensitivity as much as ∼10-fold,[60] and is essential for driving homeostatic plasticity.[68] We observed CaMKII activation coincident with βCaMKII increases (Figures 5B and 5D). Grounded in these data, the model shows

how CaMKII activity can be harnessed for homeostatic purposes, extending its classic Hebbian role.

What might synapses gain by coopting classically Hebbian mechanisms for homeostasis?

First, engaging changes in CaMKII (and CaN) activity offers heightened Ca^{2+} buffering power and faster compensation. Preventing Hebbian aspects of CaMKII mobilization in our model by blocking switchover to the β isoform caused inactivity-induced readjustment of Ca^{2+} to be weaker and slower than with Hebbian support (Figure 7D). In the steady state, the change in Ca^{2+} in response to a 10-fold variation in quantal frequency was 9.3-fold with CPARs at maximum, 4.0-fold with no CPARs, and only 2.0-fold when CPARs were feedback regulated by CaN and CaMKII (Figure 7D). Thus, "Hebbian" machinery boosts the steady-state properties and dynamics of homeostatic adaptation.

Second, the α→βCaMKII switch protects synaptic readiness for future rapid synaptic strengthening. Ca^{2+}-dependent expression of the βCaMKII isoform recalibrates the level of Ca^{2+} needed to activate the CaMKII holoenzyme (Figure 7B), thus autoregulating the Ca^{2+} sensitivity of "Hebbian" elements in a metaplastic fashion. The proportion of βCaMKII altered the relationship between input rate and Ca^{2+} levels (Figure S9B). For low %βCaMKII, steady-state Ca^{2+} exhibited bistability, but only at a high input rate. As %βCaMKII increased, lower input rates could suffice to elicit bistability (Figure S9B). Thus, the capability for synaptic plasticity is itself under homeostatic control and represents a form of metaplasticity reminiscent of sliding threshold models.[3,40,69–71]

Third, synaptic localization of CaN supports its participation in both Hebbian and homeostatic contexts. Postsynaptically anchored CaN[25] plays a dominant role in LTD as another "Hebbian" mechanism that uses positive feedback.[71] CaN-driven synaptic homeostasis[9,10] could be conceptualized as "dedepression" or removal of a tonic LTD. By upregulating CPARs after a TTX-induced decrease in network activity, CaN deactivation can also contribute to readying synapses for synaptic plasticity on demand. CaN may directly control GluA1 phosphorylation[10,25] or regulate retinoic acid synthesis.[9] Our experiments add to this emerging framework by demonstrating the joint operation of CaN and CaMKII as opposing limbs of Ca_V1-related signaling (Figure 7E). When both enzymes were blocked by FK506 and KN-93, respectively, changes in mEPSCs were completely prevented (Figure 6).

Fourth, the use of Hebbian mechanisms for homeostasis at synapses helps mobilize synapse-to-nucleus signaling for further homeostatic ends. Multiple aspects of local postsynaptic signaling are redeployed for more global purposes. CPAR-, LTCC-, CaN-, and CaMKII-dependent signal transduction triggers the translocation of protein messenger molecules to the nucleus to control alternative mRNA splicing, thus driving changes in BK (big potassium) channel variants,[48] in addition to its role in activity-coupled gene transcription.[72] PhTx block of CPARs prevents such adjustments of intrinsic properties,[48] suggesting that postsynaptic Ca^{2+} homeostasis serves as the initiator of neuron-wide autoregulation, including excitability, patterning, and firing.[73–76]

In summary, leveraging canonically Hebbian mechanisms for synaptic homeostasis offers multiple advantages for synaptic and neuronal function.

Cav1.2 channels act as homeostatic effectors: Implications for intact circuits and insights from an autism-associated mutation

Our studies of the TiS G406R mutation[51,52,58,77,78] suggest that $Ca_V1.2$ LTCCs act as effectors for homeostatic adaptation. LTCCs interact with multiple postsynaptic elements such as AKAP67/150,[79] protein kinase A (PKA),[26,80] CaN,[79] and CaMKII[15] and play central roles in signaling synaptic activity to the nucleus.[72] The G406R mutation results in altered voltage activation, impaired inactivation, increased Ca^{2+} flux,[51,52,58] and exaggerated VΔC,[15] prompting our study of accompanying inactivity-driven changes in synaptic function. We found dynamic shifts in fluctuations of CPAR-mediated mEPSC amplitude (Figures 2 and 3) and larger TTX-induced peaks of pCaMKII activation and βCaMKII in spines (Figure 5); this was consistent with $Ca_V1.2$ VΔC favoring local CaMKII accumulation and activation.[15] Notably, TTX-treated TiS neurons did not exhibit exaggerated mEPSC amplitudes, nor were differences observed at baseline (Figure 2). In TiS, enhancement of FK506-induced changes in mEPSCs (Figure 4) indicates that increased pCaMKII activity is counterbalanced by higher basal CaN activity (Figure 7D). The TiS mutation provides genetic evidence that $Ca_V1.2$ functions as an effector, recruiting CaMKII and CaN to implement synaptic homeostasis.

As an effector, $Ca_V1.2$ channels may be an integral component of a Ca^{2+}-dependent phosphorylation system coordinating slow synaptic modifications *in vivo* during sleep[81] and hibernation.[82] The synaptic homeostasis hypothesis proposes that a central function of sleep is to renormalize synapses after potentiation during waking hours.[83] Across the sleep-wake cycle in cortex, changes are found in mEPSC frequency and amplitude,[84] and in the synaptic phosphoproteome.[85] Intriguingly, all of the molecular players in our study, α- and βCaMKII, $Ca_V1.2$, CaN, and GluA1, exhibit fluctuations in phosphorylation across the sleep-wake cycle.[85] This implicates our Ca^{2+}-dependent phosphorylation feedback mechanism in supporting sleep-wake synaptic renormalization. Given that neurological conditions, including autism, involve sleep disruption,[86] it is intriguing that the dynamics of synaptic adaptations were altered in neurons bearing the TiS mutation, the basis of a syndromic form of autism spectrum disorders. We note that fluctuations in synaptic weight are not seen in *ex vivo* recordings in slices from animals subjected to sensory deprivation.[2,87] However, this conforms with our modeling of effects of mild input reductions (Figure S9D), given the only partial loss of synaptic input in sensory deprivation experiments.

A role for presynaptic adaptation in responses to homeostatic perturbations *in vitro* and *in vivo*

We observed significant TTX-induced fluctuations in mEPSC frequency (Figures 1 and 2), suggesting that presynaptic homeostatic responses are also non-monotonic.[88] CPARs and βCaMKII influence presynaptic adaptations to inactivity via retrograde signaling.[28,68,89,90] Retrograde signaling links

postsynaptic interventions to presynaptic modifications of vesicle release at neuromuscular junctions and central synapses,[91] in invertebrates,[92] and in vertebrates *in vivo*,[93] and is evident even with complete action potential blockade.[94] Thus, our observation of a TTX-induced oscillation in presynaptic efficacy has precedent. Curiously, *in vivo* removal of visual input to layer 5 cortical neurons first decreases mEPSC frequency and returns close to baseline before mEPSC amplitude increases.[2] Likewise, when we remove the presynaptic oscillation in our model, the late stage of the homeostatic response does not occur (Figures 7D and S9C). This suggests that the inactivity-driven increase in mEPSC at 24–48 h arises from both pre- and postsynaptic elements responding together.

Various mechanisms could be involved in the hypothesized post- to pre- back to post communication,[95] including postsynaptic mammalian target of rapamycin complex 1 (mTORC1)-mediated brain-derived neurotrophic factor (BDNF) signaling.[36,96] Such a scenario could involve translational control through mTORC1[97] and retinoic acid,[9] and then act through Ca^{2+}-mediated BDNF release[68,90] to signal back to the presynaptic compartment.[89] Another possible scheme invokes retrograde messengers such as nitric oxide[98] produced by nitric oxide synthase, which is also regulated by CaMKII[99–101] and CaN.[102,103] Further questions about the mechanism can now be addressed more effectively by combining perspectives on "Hebbian" and homeostatic synaptic plasticity and appreciating their aspects of dynamic overlap.

Limitations of the study

Although *in vitro* and *in silico* approaches are more experimentally tractable, enabling closed-loop mechanistic dissections, our study lacks a directly analogous *in vivo* manipulation. Similarly, TTX blocks all spiking, whereas synaptic activity independent of action potential release is maintained. Endogenous and experimental activity changes *in vivo* do not result in activity reductions to the same degree as our pharmacological manipulation, which we could limitedly address in our model (Figure S9D). Our experiments did not explore the results of prolonged activity increases or the detailed mechanism by which inactivity-driven CaMKII activation increases AMPAR weight.[104,105] To design a sufficiently simple model to qualitatively capture the hypothesized interactions, we made several idealizations, outlined in our model supplement.

STAR★METHODS

Detailed methods are provided in the online version of this paper and include the following:

- KEY RESOURCES TABLE
- RESOURCE AVAILABILITY
  - Lead contact
  - Materials availability
  - Data and code availability
- EXPERIMENTAL MODEL AND STUDY PARTICIPANT DETAILS
  - Animal lines
- METHOD DETAILS
  - Primary cortical culturing
  - Electrophysiological recordings and analysis
  - Imaging
- QUANTIFICATION AND STATISTICAL ANALYSIS
  - Statistical tests for group effects
  - Linear regression
  - Model supplement
  - Model limitations

AUTHOR CONTRIBUTIONS

Conceptualization: S. Sun, D.L., B.L., and R.T. Methodology: S. Sun, D.L., N.C., B.S., and R.T. Investigation: S. Sun and B.S. Data curation: S. Sun, D.L., N.C., and B.S. Formal analysis: S. Sun, D.L., and N.M. Validation: S. Sun and R.T. Writing – original draft: S. Sun, D.L., and R.T. Writing – review & editing: S. Sun, D.L., B.L., N.M., N.C., J.R., G.B., and R.T. Visualization: S. Sun and R.T. Resources: B.L., N.C., S. Sanchez, and G.T. Software: D.L. and N.C. Funding acquisition: S. Sun and R.T. Supervision: J.R., G.B., and R.T. Project administration: S. Sanchez and G.T.

REFERENCES

1. Turrigiano, G.G., Leslie, K.R., Desai, N.S., Rutherford, L.C., and Nelson, S.B. (1998). Activity-dependent scaling of quantal amplitude in neocortical neurons. Nature *391*, 892–896. https://doi.org/10.1038/36103.

2. Keck, T., Keller, G.B., Jacobsen, R.I., Eysel, U.T., Bonhoeffer, T., and Hübener, M. (2013). Synaptic scaling and homeostatic plasticity in the mouse visual cortex in vivo. Neuron *80*, 327–334. https://doi.org/10.1016/j.neuron.2013.08.018.

3. Lee, H.-K., and Kirkwood, A. (2019). Mechanisms of Homeostatic Synaptic Plasticity in vivo. Front. Cell. Neurosci. *13*, 520. https://doi.org/10.3389/fncel.2019.00520.

4. Lee, K.F.H., Soares, C., and Béïque, J.C. (2014). Tuning into diversity of homeostatic synaptic plasticity. Neuropharmacology *78*, 31–37. https://doi.org/10.1016/j.neuropharm.2013.03.016.

5. Barria, A., Muller, D., Derkach, V., Griffith, L.C., and Soderling, T.R. (1997). Regulatory Phosphorylation of AMPA-Type Glutamate Receptors by CaM-KII During Long-Term Potentiation. Science *276*, 2042–2045. https://doi.org/10.1126/science.276.5321.2042.

6. Hell, J.W. (2014). CaMKII: claiming center stage in postsynaptic function and organization. Neuron *81*, 249–265. https://doi.org/10.1016/j.neuron.2013.12.024.

7. Lee, H.K., Kameyama, K., Huganir, R.L., and Bear, M.F. (1998). NMDA induces long-term synaptic depression and dephosphorylation of the GluR1 subunit of AMPA receptors in hippocampus. Neuron *21*, 1151–1162. https://doi.org/10.1016/s0896-6273(00)80632-7.

8. Lisman, J., Yasuda, R., and Raghavachari, S. (2012). Mechanisms of CaMKII action in long-term potentiation. Nat. Rev. Neurosci. *13*, 169–182. https://doi.org/10.1038/nrn3192.

9. Arendt, K.L., Zhang, Z., Ganesan, S., Hintze, M., Shin, M.M., Tang, Y., Cho, A., Graef, I.A., and Chen, L. (2015). Calcineurin mediates homeostatic synaptic plasticity by regulating retinoic acid synthesis. Proc. Natl. Acad. Sci. USA *112*, E5744–E5752. https://doi.org/10.1073/pnas.1510239112.

10. Kim, S., and Ziff, E.B. (2014). Calcineurin mediates synaptic scaling via synaptic trafficking of Ca2+-permeable AMPA receptors. PLoS Biol. *12*, e1001900. https://doi.org/10.1371/journal.pbio.1001900.

11. Thiagarajan, T.C., Lindskog, M., Malgaroli, A., and Tsien, R.W. (2007). LTP and adaptation to inactivity: Overlapping mechanisms and implications for metaplasticity. Neuropharmacology *52*, 156–175. https://doi.org/10.1016/j.neuropharm.2006.07.030.

12. Hudmon, A., Schulman, H., Kim, J., Maltez, J.M., Tsien, R.W., and Pitt, G.S. (2005). CaMKII tethers to L-type Ca2+ channels, establishing a local and dedicated integrator of Ca2+ signals for facilitation. J. Cell Biol. *171*, 537–547. https://doi.org/10.1083/jcb.200505155.

13. Murphy, J.G., Sanderson, J.L., Gorski, J.A., Scott, J.D., Catterall, W.A., Sather, W.A., and Dell'Acqua, M.L. (2014). AKAP-anchored PKA maintains neuronal L-type calcium channel activity and NFAT transcriptional signaling. Cell Rep. *7*, 1577–1588. https://doi.org/10.1016/j.celrep.2014.04.027.

14. Bauer, E.P., Schafe, G.E., and LeDoux, J.E. (2002). NMDA receptors and L-type voltage-gated calcium channels contribute to long-term potentiation and different components of fear memory formation in the lateral amygdala. J. Neurosci. *22*, 5239–5249. https://doi.org/10.1523/jneurosci.22-12-05239.2002.

15. Li, B., Tadross, M.R., and Tsien, R.W. (2016). Sequential ionic and conformational signaling by calcium channels drives neuronal gene expression. Science *351*, 863–867. https://doi.org/10.1126/science.aad3647.

16. Wheeler, D.G., Barrett, C.F., Groth, R.D., Safa, P., and Tsien, R.W. (2008). CaMKII locally encodes L-type channel activity to signal to nuclear CREB in excitation–transcription coupling. J. Cell Biol. *183*, 849–863. https://doi.org/10.1083/jcb.200805048.

17. O'Leary, T., van Rossum, M.C.W., and Wyllie, D.J.A. (2010). Homeostasis of intrinsic excitability in hippocampal neurones: dynamics and mechanism of the response to chronic depolarization. J. Physiol. *588*, 157–170. https://doi.org/10.1113/jphysiol.2009.181024.

18. Slutsky, I., Sadeghpour, S., Li, B., and Liu, G. (2004). Enhancement of synaptic plasticity through chronically reduced Ca2+ flux during uncorrelated activity. Neuron *44*, 835–849. https://doi.org/10.1016/j.neuron.2004.11.013.

19. Chater, T.E., and Goda, Y. (2014). The role of AMPA receptors in postsynaptic mechanisms of synaptic plasticity. Front. Cell. Neurosci. *8*, 401. https://doi.org/10.3389/fncel.2014.00401.

20. Diering, G.H., and Huganir, R.L. (2018). The AMPA Receptor Code of Synaptic Plasticity. Neuron *100*, 314–329. https://doi.org/10.1016/j.neuron.2018.10.018.

21. Hayashi, Y., Shi, S.H., Esteban, J.A., Piccini, A., Poncer, J.C., and Malinow, R. (2000). Driving AMPA receptors into synapses by LTP and CaMKII: requirement for GluR1 and PDZ domain interaction. Science *287*, 2262–2267. https://doi.org/10.1126/science.287.5461.2262.

22. Park, P., Kang, H., Sanderson, T.M., Bortolotto, Z.A., Georgiou, J., Zhuo, M., Kaang, B.-K., and Collingridge, G.L. (2018). The Role of Calcium-Permeable AMPARs in Long-Term Potentiation at Principal Neurons in the Rodent Hippocampus. Front. Synaptic Neurosci. *10*, 42. https://doi.org/10.3389/fnsyn.2018.00042.

23. Sanderson, J.L., Gorski, J.A., and Dell'Acqua, M.L. (2016). NMDA Receptor-Dependent LTD Requires Transient Synaptic Incorporation of Ca2+-Permeable AMPARs Mediated by AKAP150-Anchored PKA and Calcineurin. Neuron *89*, 1000–1015. https://doi.org/10.1016/j.neuron.2016.01.043.

24. Purkey, A.M., Woolfrey, K.M., Crosby, K.C., Stich, D.G., Chick, W.S., Aoto, J., and Dell'Acqua, M.L. (2018). AKAP150 Palmitoylation Regulates Synaptic Incorporation of Ca2+-Permeable AMPA Receptors to Control LTP. Cell Rep. *25*, 974–987.e4. https://doi.org/10.1016/j.celrep.2018.09.085.

25. Sanderson, J.L., Scott, J.D., and Dell'Acqua, M.L. (2018). Control of Homeostatic Synaptic Plasticity by AKAP-Anchored Kinase and Phosphatase Regulation of Ca2+-Permeable AMPA Receptors. J. Neurosci. *38*, 2863–2876. https://doi.org/10.1523/JNEUROSCI.2362-17.2018.

26. Diering, G.H., Gustina, A.S., and Huganir, R.L. (2014). PKA-GluA1 coupling via AKAP5 controls AMPA receptor phosphorylation and cell-surface targeting during bidirectional homeostatic plasticity. Neuron *84*, 790–805. https://doi.org/10.1016/j.neuron.2014.09.024.

27. Soares, C., Lee, K.F.H., Nassrallah, W., and Béïque, J.C. (2013). Differential subcellular targeting of glutamate receptor subtypes during homeostatic synaptic plasticity. J. Neurosci. *33*, 13547–13559. https://doi.org/10.1523/JNEUROSCI.1873-13.2013.

28. Thiagarajan, T.C., Lindskog, M., and Tsien, R.W. (2005). Adaptation to synaptic inactivity in hippocampal neurons. Neuron *47*, 725–737. https://doi.org/10.1016/j.neuron.2005.06.037.

29. Wierenga, C.J., Ibata, K., and Turrigiano, G.G. (2005). Postsynaptic Expression of Homeostatic Plasticity at Neocortical Synapses. J. Neurosci. *25*, 2895–2905. https://doi.org/10.1523/jneurosci.5217-04.2005.

30. Gainey, M.A., Hurvitz-Wolff, J.R., Lambo, M.E., and Turrigiano, G.G. (2009). Synaptic scaling requires the GluR2 subunit of the AMPA receptor. J. Neurosci. *29*, 6479–6489. https://doi.org/10.1523/JNEUROSCI.3753-08.2009.

31. Turrigiano, G. (2012). Homeostatic synaptic plasticity: local and global mechanisms for stabilizing neuronal function. Cold Spring Harbor Perspect. Biol. *4*, a005736. https://doi.org/10.1101/cshperspect.a005736.

32. Coultrap, S.J., and Bayer, K.U. (2012). CaMKII regulation in information processing and storage. Trends Neurosci. *35*, 607–618. https://doi.org/10.1016/j.tins.2012.05.003.

33. Fujii, H., Inoue, M., Okuno, H., Sano, Y., Takemoto-Kimura, S., Kitamura, K., Kano, M., and Bito, H. (2013). Nonlinear decoding and asymmetric representation of neuronal input information by CaMKIIα and calcineurin. Cell Rep. *3*, 978–987. https://doi.org/10.1016/j.celrep.2013.03.033.

34. Lee, S.-J.R., Escobedo-Lozoya, Y., Szatmari, E.M., and Yasuda, R. (2009). Activation of CaMKII in single dendritic spines during long-term potentiation. Nature *458*, 299–304. https://doi.org/10.1038/nature07842.

35. Makino, H., and Malinow, R. (2009). AMPA receptor incorporation into synapses during LTP: the role of lateral movement and exocytosis. Neuron *64*, 381–390. https://doi.org/10.1016/j.neuron.2009.08.035.

36. Henry, F.E., Wang, X., Serrano, D., Perez, A.S., Carruthers, C.J.L., Stuenkel, E.L., and Sutton, M.A. (2018). A Unique Homeostatic Signaling Pathway Links Synaptic Inactivity to Postsynaptic mTORC1. J. Neurosci. *38*, 2207–2225. https://doi.org/10.1523/jneurosci.1843-17.2017.

37. Adesnik, H., Nicoll, R.A., and England, P.M. (2005). Photoinactivation of native AMPA receptors reveals their real-time trafficking. Neuron *48*, 977–985. https://doi.org/10.1016/j.neuron.2005.11.030.

38. Ibata, K., Sun, Q., and Turrigiano, G.G. (2008). Rapid synaptic scaling induced by changes in postsynaptic firing. Neuron 57, 819–826. https://doi.org/10.1016/j.neuron.2008.02.031.

39. Schaukowitch, K., Reese, A.L., Kim, S.-K., Kilaru, G., Joo, J.-Y., Kavalali, E.T., and Kim, T.-K. (2017). An Intrinsic Transcriptional Program Underlying Synaptic Scaling during Activity Suppression. Cell Rep. 18, 1512–1526. https://doi.org/10.1016/j.celrep.2017.01.033.

40. Keck, T., Hübener, M., and Bonhoeffer, T. (2017). Interactions between synaptic homeostatic mechanisms: an attempt to reconcile BCM theory, synaptic scaling, and changing excitation/inhibition balance. Curr. Opin. Neurobiol. 43, 87–93. https://doi.org/10.1016/j.conb.2017.02.003.

41. Izhikevich, E.M. (2007). Dynamical Systems in Neuroscience (MIT Press).

42. O'Leary, T., and Wyllie, D.J.A. (2011). Neuronal homeostasis: time for a change? J. Physiol. 589, 4811–4826. https://doi.org/10.1113/jphysiol.2011.210179.

43. Zenke, F., and Gerstner, W. (2017). Hebbian plasticity requires compensatory processes on multiple timescales. Philos. Trans. R. Soc. Lond. B Biol. Sci. 372, 20160259. https://doi.org/10.1098/rstb.2016.0259.

44. Buonomano, D.V. (2005). A learning rule for the emergence of stable dynamics and timing in recurrent networks. J. Neurophysiol. 94, 2275–2283. https://doi.org/10.1152/jn.01250.2004.

45. Harnack, D., Pelko, M., Chaillet, A., Chitour, Y., and van Rossum, M.C.W. (2015). Stability of Neuronal Networks with Homeostatic Regulation. PLoS Comput. Biol. 11, e1004357. https://doi.org/10.1371/journal.pcbi.1004357.

46. Toyoizumi, T., Kaneko, M., Stryker, M.P., and Miller, K.D. (2014). Modeling the dynamic interaction of Hebbian and homeostatic plasticity. Neuron 84, 497–510. https://doi.org/10.1016/j.neuron.2014.09.036.

47. Yeung, L.C., Shouval, H.Z., Blais, B.S., and Cooper, L.N. (2004). Synaptic homeostasis and input selectivity follow from a calcium-dependent plasticity model. Proc. Natl. Acad. Sci. USA 101, 14943–14948. https://doi.org/10.1073/pnas.0405555101.

48. Li, B., Suutari, B.S., Sun, S.D., Luo, Z., Wei, C., Chenouard, N., Mandelberg, N.J., Zhang, G., Wamsley, B., Tian, G., et al. (2020). Neuronal Inactivity Co-opts LTP Machinery to Drive Potassium Channel Splicing and Homeostatic Spike Widening. Cell 181, 1547–1565.e15. https://doi.org/10.1016/j.cell.2020.05.013.

49. Zenke, F., Gerstner, W., and Ganguli, S. (2017). The temporal paradox of Hebbian learning and homeostatic plasticity. Curr. Opin. Neurobiol. 43, 166–176. https://doi.org/10.1016/j.conb.2017.03.015.

50. Thiagarajan, T.C., Piedras-Renteria, E.S., and Tsien, R.W. (2002). alpha-and betaCaMKII. Inverse regulation by neuronal activity and opposing effects on synaptic strength. Neuron 36, 1103–1114. https://doi.org/10.1016/s0896-6273(02)01049-8.

51. Dick, I.E., Joshi-Mukherjee, R., Yang, W., and Yue, D.T. (2016). Arrhythmogenesis in Timothy Syndrome is associated with defects in Ca(2+)-dependent inactivation. Nat. Commun. 7, 10370. https://doi.org/10.1038/ncomms10370.

52. Splawski, I., Timothy, K.W., Sharpe, L.M., Decher, N., Kumar, P., Bloise, R., Napolitano, C., Schwartz, P.J., Joseph, R.M., Condouris, K., et al. (2004). Ca(V)1.2 calcium channel dysfunction causes a multisystem disorder including arrhythmia and autism. Cell 119, 19–31. https://doi.org/10.1016/j.cell.2004.09.011.

53. Turrigiano, G.G., and Nelson, S.B. (1998). Thinking globally, acting locally: AMPA receptor turnover and synaptic strength. Neuron 21, 933–935. https://doi.org/10.1016/s0896-6273(00)80607-8.

54. Turrigiano, G.G., and Nelson, S.B. (2004). Homeostatic plasticity in the developing nervous system. Nat. Rev. Neurosci. 5, 97–107. https://doi.org/10.1038/nrn1327.

55. Ancona Esselmann, S.G., Díaz-Alonso, J., Levy, J.M., Bemben, M.A., and Nicoll, R.A. (2017). Synaptic homeostasis requires the membrane-proximal carboxy tail of GluA2. Proc. Natl. Acad. Sci. USA 114, 13266–13271. https://doi.org/10.1073/pnas.1716022114.

56. Bader, P.L., Faizi, M., Kim, L.H., Owen, S.F., Tadross, M.R., Alfa, R.W., Bett, G.C.L., Tsien, R.W., Rasmusson, R.L., and Shamloo, M. (2011). Mouse model of Timothy syndrome recapitulates triad of autistic traits. Proc. Natl. Acad. Sci. USA 108, 15432–15437. https://doi.org/10.1073/pnas.1112667108.

57. Sztainberg, Y., and Zoghbi, H.Y. (2016). Lessons learned from studying syndromic autism spectrum disorders. Nat. Neurosci. 19, 1408–1417. https://doi.org/10.1038/nn.4420.

58. Splawski, I., Timothy, K.W., Decher, N., Kumar, P., Sachse, F.B., Beggs, A.H., Sanguinetti, M.C., and Keating, M.T. (2005). Severe arrhythmia disorder caused by cardiac L-type calcium channel mutations. Proc. Natl. Acad. Sci. USA 102, 8089–8088. https://doi.org/10.1073/pnas.0502506102.

59. Mosbacher, J., Schoepfer, R., Monyer, H., Burnashev, N., Seeburg, P.H., and Ruppersberg, J.P. (1994). A molecular determinant for submillisecond desensitization in glutamate receptors. Science 266, 1059–1062. https://doi.org/10.1126/science.7973663.

60. Brocke, L., Chiang, L.W., Wagner, P.D., and Schulman, H. (1999). Functional implications of the subunit composition of neuronal CaM kinase II. J. Biol. Chem. 274, 22713–22722. https://doi.org/10.1074/jbc.274.32.22713.

61. Burgin, K.E., Waxham, M.N., Rickling, S., Westgate, S.A., Mobley, W.C., and Kelly, P.T. (1990). In situ hybridization histochemistry of Ca2+/calmodulin-dependent protein kinase in developing rat brain. J. Neurosci. 10, 1788–1798.

62. Maghsoodi, B., Poon, M.M., Nam, C.I., Aoto, J., Ting, P., and Chen, L. (2008). Retinoic acid regulates RARalpha-mediated control of translation in dendritic RNA granules during homeostatic synaptic plasticity. Proc. Natl. Acad. Sci. USA 105, 16015–16020. https://doi.org/10.1073/pnas.0804801105.

63. Sanderson, J.L., Gorski, J.A., Gibson, E.S., Lam, P., Freund, R.K., Chick, W.S., and Dell'Acqua, M.L. (2012). AKAP150-Anchored Calcineurin Regulates Synaptic Plasticity by Limiting Synaptic Incorporation of Ca2+-Permeable AMPA Receptors. J. Neurosci. 32, 15036–15052. https://doi.org/10.1523/JNEUROSCI.3326-12.2012.

64. Wang, H.-L., Zhang, Z., Hintze, M., and Chen, L. (2011). Decrease in calcium concentration triggers neuronal retinoic acid synthesis during homeostatic synaptic plasticity. J. Neurosci. 31, 17764–17771. https://doi.org/10.1523/JNEUROSCI.3964-11.2011.

65. Bayer, K.U., and Schulman, H. (2019). CaM Kinase: Still Inspiring at 40. Neuron 103, 380–394. https://doi.org/10.1016/j.neuron.2019.05.033.

66. Herring, B.E., and Nicoll, R.A. (2016). Long-Term Potentiation: From CaMKII to AMPA Receptor Trafficking. Annu. Rev. Physiol. 78, 351–365. https://doi.org/10.1146/annurev-physiol-021014-071753.

67. Lee, K.Y., and Chung, H.J. (2014). NMDA receptors and L-type voltage-gated Ca2+ channels mediate the expression of bidirectional homeostatic intrinsic plasticity in cultured hippocampal neurons. Neuroscience 277, 610–623. https://doi.org/10.1016/j.neuroscience.2014.07.038.

68. Groth, R.D., Lindskog, M., Thiagarajan, T.C., Li, L., and Tsien, R.W. (2011). Beta Ca2+/CaM-dependent kinase type II triggers upregulation of GluA1 to coordinate adaptation to synaptic inactivity in hippocampal neurons. Proc. Natl. Acad. Sci. USA 108, 828–833. https://doi.org/10.1073/pnas.1018022108.

69. Abraham, W.C., and Bear, M.F. (1996). Metaplasticity: the plasticity of synaptic plasticity. Trends Neurosci. 19, 126–130. https://doi.org/10.1016/s0166-2236(96)80018-x.

70. Li, J., Park, E., Zhong, L.R., and Chen, L. (2019). Homeostatic synaptic plasticity as a metaplasticity mechanism - a molecular and cellular perspective. Curr. Opin. Neurobiol. 54, 44–53. https://doi.org/10.1016/j.conb.2018.08.010.

71. Malenka, R.C., and Bear, M.F. (2004). LTP and LTD: an embarrassment of riches. Neuron 44, 5–21. https://doi.org/10.1016/j.neuron.2004.09.012.

72. Ma, H., Khaled, H.G., Wang, X., Mandelberg, N.J., Cohen, S.M., He, X., and Tsien, R.W. (2023). Excitation-transcription coupling, neuronal gene expression and synaptic plasticity. Nat. Rev. Neurosci. *24*, 672–692. https://doi.org/10.1038/s41583-023-00742-5.

73. Fong, M.-F., Newman, J.P., Potter, S.M., and Wenner, P. (2015). Upward synaptic scaling is dependent on neurotransmission rather than spiking. Nat. Commun. *6*, 6339. https://doi.org/10.1038/ncomms7339.

74. LeMasson, G., Marder, E., and Abbott, L.F. (1993). Activity-dependent regulation of conductances in model neurons. Science *259*, 1915–1917. https://doi.org/10.1126/science.8456317.

75. Marder, E., Abbott, L.F., Turrigiano, G.G., Liu, Z., and Golowasch, J. (1996). Memory from the dynamics of intrinsic membrane currents. Proc. Natl. Acad. Sci. USA *93*, 13481–13486. https://doi.org/10.1073/pnas.93.24.13481.

76. Siegel, M., Marder, E., and Abbott, L.F. (1994). Activity-dependent current distributions in model neurons. Proc. Natl. Acad. Sci. USA *91*, 11308–11312. https://doi.org/10.1073/pnas.91.24.11308.

77. Bauer, R., Timothy, K.W., and Golden, A. (2021). Update on the Molecular Genetics of Timothy Syndrome. Front. Pediatr. *9*, 668546. https://doi.org/10.3389/fped.2021.668546.

78. Mullins, C., Fishell, G., and Tsien, R.W. (2016). Unifying Views of Autism Spectrum Disorders: A Consideration of Autoregulatory Feedback Loops. Neuron *89*, 1131–1156. https://doi.org/10.1016/j.neuron.2016.02.017.

79. Dittmer, P.J., Dell'Acqua, M.L., and Sather, W.A. (2014). Ca2+/calcineurin-dependent inactivation of neuronal L-type Ca2+ channels requires priming by AKAP-anchored protein kinase A. Cell Rep. *7*, 1410–1416. https://doi.org/10.1016/j.celrep.2014.04.039.

80. Xu, H., Ginsburg, K.S., Hall, D.D., Zimmermann, M., Stein, I.S., Zhang, M., Tandan, S., Hill, J.A., Horne, M.C., Bers, D., and Hell, J.W. (2010). Targeting of protein phosphatases PP2A and PP2B to the C-terminus of the L-type calcium channel Ca v1.2. Biochemistry *49*, 10298–10307. https://doi.org/10.1021/bi101018c.

81. Diering, G.H., Nirujogi, R.S., Roth, R.H., Worley, P.F., Pandey, A., and Huganir, R.L. (2017). Homer1a drives homeostatic scaling-down of excitatory synapses during sleep. Science *355*, 511–515. https://doi.org/10.1126/science.aai8355.

82. Zubov, T., do Amaral-Silva, L., and Santin, J.M. (2022). Inactivity and Ca2+ signaling regulate synaptic compensation in motoneurons following hibernation in American bullfrogs. Sci. Rep. *12*, 11610. https://doi.org/10.1038/s41598-022-15525-8.

83. Tononi, G., and Cirelli, C. (2003). Sleep and synaptic homeostasis: a hypothesis. Brain Res. Bull. *62*, 143–150. https://doi.org/10.1016/j.brainresbull.2003.09.004.

84. Liu, Z.-W., Faraguna, U., Cirelli, C., Tononi, G., and Gao, X.-B. (2010). Direct Evidence for Wake-Related Increases and Sleep-Related Decreases in Synaptic Strength in Rodent Cortex. J. Neurosci. *30*, 8671–8675. https://doi.org/10.1523/jneurosci.1409-10.2010.

85. Brüning, F., Noya, S.B., Bange, T., Koutsouli, S., Rudolph, J.D., Tyagarajan, S.K., Cox, J., Mann, M., Brown, S.A., and Robles, M.S. (2019). Sleep-wake cycles drive daily dynamics of synaptic phosphorylation. Science *366*, eaav3617. https://doi.org/10.1126/science.aav3617.

86. Cohen, S., Conduit, R., Lockley, S.W., Rajaratnam, S.M., and Cornish, K.M. (2014). The relationship between sleep and behavior in autism spectrum disorder (ASD): a review. J. Neurodev. Disord. *6*, 44. https://doi.org/10.1186/1866-1955-6-44.

87. Maffei, A., Nelson, S.B., and Turrigiano, G.G. (2004). Selective reconfiguration of layer 4 visual cortical circuitry by visual deprivation. Nat. Neurosci. *7*, 1353–1359. https://doi.org/10.1038/nn1351.

88. Murthy, V.N., Schikorski, T., Stevens, C.F., and Zhu, Y. (2001). Inactivity produces increases in neurotransmitter release and synapse size. Neuron *32*, 673–682. https://doi.org/10.1016/s0896-6273(01)00500-1.

89. Jakawich, S.K., Nasser, H.B., Strong, M.J., McCartney, A.J., Perez, A.S., Rakesh, N., Carruthers, C.J.L., and Sutton, M.A. (2010). Local presynaptic activity gates homeostatic changes in presynaptic function driven by dendritic BDNF synthesis. Neuron *68*, 1143–1158. https://doi.org/10.1016/j.neuron.2010.11.034.

90. Lindskog, M., Li, L., Groth, R.D., Poburko, D., Thiagarajan, T.C., Han, X., and Tsien, R.W. (2010). Postsynaptic GluA1 enables acute retrograde enhancement of presynaptic function to coordinate adaptation to synaptic inactivity. Proc. Natl. Acad. Sci. USA *107*, 21806–21811. https://doi.org/10.1073/pnas.1016399107.

91. Davis, G.W., and Müller, M. (2015). Homeostatic control of presynaptic neurotransmitter release. Annu. Rev. Physiol. *77*, 251–270. https://doi.org/10.1146/annurev-physiol-021014-071740.

92. Frank, C.A. (2014). Homeostatic plasticity at the Drosophila neuromuscular junction. Neuropharmacology *78*, 63–74. https://doi.org/10.1016/j.neuropharm.2013.06.015.

93. Wang, X., Wang, Q., Engisch, K.L., and Rich, M.M. (2010). Activity-dependent regulation of the binomial parameters p and n at the mouse neuromuscular junction in vivo. J. Neurophysiol. *104*, 2352–2358. https://doi.org/10.1152/jn.00460.2010.

94. Kavalali, E.T. (2015). The mechanisms and functions of spontaneous neurotransmitter release. Nat. Rev. Neurosci. *16*, 5–16. https://doi.org/10.1038/nrn3875.

95. Tokuoka, H., and Goda, Y. (2008). Activity-dependent coordination of presynaptic release probability and postsynaptic GluR2 abundance at single synapses. Proc. Natl. Acad. Sci. USA *105*, 14656–14661. https://doi.org/10.1073/pnas.0805705105.

96. Henry, F.E., McCartney, A.J., Neely, R., Perez, A.S., Carruthers, C.J.L., Stuenkel, E.L., Inoki, K., and Sutton, M.A. (2012). Retrograde changes in presynaptic function driven by dendritic mTORC1. J. Neurosci. *32*, 17128–17142. https://doi.org/10.1523/JNEUROSCI.2149-12.2012.

97. Wang, C.S., Kavalali, E.T., and Monteggia, L.M. (2021). BDNF signaling in context: From synaptic regulation to psychiatric disorders. Cell *185*, 62–76. https://doi.org/10.1016/j.cell.2021.12.003.

98. Chenouard, N., Xuan, F., and Tsien, R.W. (2020). Synaptic vesicle traffic is supported by transient actin filaments and regulated by PKA and NO. Nat. Commun. *11*, 5318. https://doi.org/10.1038/s41467-020-19120-1.

99. Araki, S., Osuka, K., Takata, T., Tsuchiya, Y., and Watanabe, Y. (2020). Coordination between Calcium/Calmodulin-Dependent Protein Kinase II and Neuronal Nitric Oxide Synthase in Neurons. Int. J. Mol. Sci. *21*, 7997. https://doi.org/10.3390/ijms21217997.

100. Komeima, K., Hayashi, Y., Naito, Y., and Watanabe, Y. (2000). Inhibition of Neuronal Nitric-oxide Synthase by Calcium/Calmodulin-dependent Protein Kinase IIα through Ser847 Phosphorylation in NG108-15 Neuronal Cells. J. Biol. Chem. *275*, 28139–28143. https://doi.org/10.1074/jbc.m003198200.

101. Watanabe, Y., Song, T., Sugimoto, K., Horii, M., Araki, N., Tokumitsu, H., Tezuka, T., Yamamoto, T., and Tokuda, M. (2003). Post-synaptic density-95 promotes calcium/calmodulin-dependent protein kinase II-mediated Ser847 phosphorylation of neuronal nitric oxide synthase. Biochem. J. *372*, 465–471. https://doi.org/10.1042/bj20030380.

102. Dawson, T.M., Steiner, J.P., Dawson, V.L., Dinerman, J.L., Uhl, G.R., and Snyder, S.H. (1993). Immunosuppressant FK506 enhances phosphorylation of nitric oxide synthase and protects against glutamate neurotoxicity. Proc. Natl. Acad. Sci. U.S.A. *90*, 9808–9812. https://doi.org/10.1073/pnas.90.21.9808.

103. Rameau, G.A., Chiu, L.-Y., and Ziff, E.B. (2004). Bidirectional regulation of neuronal nitric-oxide synthase phosphorylation at serine 847 by the N-methyl-D-aspartate receptor. J. Biol. Chem. *279*, 14307–14314. https://doi.org/10.1074/jbc.M311103200.

104. Arendt, K.L., Zhang, Y., Jurado, S., Malenka, R.C., Südhof, T.C., and Chen, L. (2015). Retinoic Acid and LTP Recruit Postsynaptic AMPA

Receptors Using Distinct SNARE-Dependent Mechanisms. Neuron *86*, 442–456. https://doi.org/10.1016/j.neuron.2015.03.009.

105. Tullis, J.E., Larsen, M.E., Rumian, N.L., Freund, R.K., Boxer, E.E., Brown, C.N., Coultrap, S.J., Schulman, H., Aoto, J., Dell'Acqua, M.L., and Bayer, K.U. (2023). LTP induction by structural rather than enzymatic functions of CaMKII. Nature *621*, 146–153. https://doi.org/10.1038/s41586-023-06465-y.

106. Bett, G.C., Lis, A., Wersinger, S.R., Baizer, J.S., Duffey, M.E., and Rasmusson, R.L. (2012). A Mouse Model of Timothy Syndrome: a Complex Autistic Disorder Resulting from a Point Mutation in Cav1.2. N. Am. J. Med. Sci. *5*, 135–140. https://doi.org/10.7156/najms.2012.053135.

STAR★METHODS

KEY RESOURCES TABLE

REAGENT or RESOURCE	SOURCE	IDENTIFIER
Antibodies		
anti-GluR1 (rabbit)	Millipore	Cat#05-855R, RRID:AB_10015249
anti-GluR1 (rabbit)	Calbiochem	Cat#04–855, RRID:AB_1977216
anti-pCaMKII (rabbit)	Cell Signaling Technology	Cat#12716S, RRID:AB_2713889
anti-PSD95 (mouse IgG2a)	Biolegend	Cat#810401, RRID:AB_2564750
anti-PSD95 (mouse)	Synaptic Systems	Cat#124011, RRID:AB_10804286
anti-PSD95 (rabbit)	Synaptic Systems	Cat#124002, RRID:AB_887760
anti-PSD95 (goat)	AbCam	Cat#AB12093, RRID:AB_298846
anti-MAP2 (guinea pig)	Synaptic Systems	Cat# 188004, RRID:AB_2138181
anti-CaMKII-alpha (rabbit)	AbCam	Cat# ab131468, RRID:AB_11157799
anti-CaMKII-beta (mouse)	AbCam	Cat#ab89197, RRID:AB_2040678
Chemicals, peptides, and recombinant proteins		
Tetrodotoxin	Alomone Labs	Cat#T-550
Philanthotoxin	Cayman Chemical Co.	Cat#14607
FK506	Fisher Scientific	Cat#AAJ63571ME
KN-93	Fisher Scientific	Cat#42-271-11MG
Deposited data		
Experimental Data and Analysis Code	Open Science Framework	https://doi.org/10.17605/OSF.IO/SDVG6
Modeling Code	GitHub	https://github.com/dlevenstein/SunLevenstein2024
Experimental models: Organisms/strains		
TS2-neo	In-Genious Targeting Laboratory, Stony Brook, NY; The Jackson Laboratory	Cat#019547 RRID:IMSR_JAX:019547
Software and algorithms		
Prism (versions 8, 9, and 10)	GraphPad	https://www.graphpad.com
MATLAB	Mathworks	https://www.mathworks.com
pClamp 10	Molecular Devices	https://www.moleculardevices.com
ICY	Icy OpenSource	https://icy.bioimageanalysis.org

RESOURCE AVAILABILITY

Lead contact
Further information and requests for resources and reagents should be addressed to Lead Contact, Richard W. Tsien (richard.tsien@nyulangone.org).

Materials availability
This study did not generate new unique reagents.

Data and code availability
- All data reported in this paper will be shared by the lead contact upon request.
- All experimental data and analysis code and has been deposited on OSF and is publicly available on date of publication. DOIs are listed in the key resources table.
- All modeling code has been deposited on GitHub and is publicly available on date of publication. Links are listed in the key resources table.
- Any additional information required to reanalyze the data reported in this paper is available from the lead contact upon request.

EXPERIMENTAL MODEL AND STUDY PARTICIPANT DETAILS

Animal lines

TS2-neo mice were originally generated by In-Genious Targeting Laboratory, Stony Brook, NY. Following the original nomenclature by Splawski et al., 2004. TS2-neo mice express the Gly-to-Arg mutation at position 406 in exon 8 of the *CACNA1C* gene. All cultures were made from dissociated cortices on P0 from TS2-neo heterozygotes crossed to WT, CB57BL/6 WT giving rise to litters with both WT and TS2-neo genotypes. All animals used were genotyped at P0.

METHOD DETAILS

Primary cortical culturing

Cultures were prepared from cortices dissected from P0-P1 mice taken from CB57BL/6 WT and heterozygous TS2-neo crosses. TS2-neo mice are available and as described in[56,106] and detailed in Animal Lines section. Litters were sex-mixed to minimize potential sex variability and genotyped for the G406R mutation day of dissection and separated between WT and TS2-neo cortices. Cortices were cultured using the methods described previously[15] with slight modifications. Briefly, WT and TS2 cortices were separately washed twice in ice-cold modified HBSS (4.2 mM $NaHCO_3$ and 1mM HEPES, pH 7.35, 300 mOsm) containing 20% fetal bovine serum (FBS). Samples were washed and digested for 8 min in a papain solution (2.5 mL HBSS +145 U papain) at 37°C. 8 μL of DNase I (0.2 M), 0.5mM $CaCl_2$ and 1mM MgCl2 was added after for an additional 3 min. Digestion was ceased by adding 5 mL of modified HBSS containing 20% FBS. After addition washing, tissue was triturated using fire polished pasteur pipettes of decreasing diameter with 1 mL of dissociation solution (HBSS +8 μL of DNase I (0.2 M)). The cell suspension was pelleted twice by centrifugation (10 min at 1000 RPM) and 4°C, first with 500 μL of 4% BSA at the bottom of the tube, with an additional 1 mL dissociation solution trituration with a 1000μL pipette trituration in between. The pellet was then filtered with a 70μm cell strainer, and plated on 12 mm diameter coverslips coated with poly-L-lysine. Cells were counted such that culture density was approximately 90,000 cells per coverslip. Cultures were maintained in NbActiv4 (BrainBits) at 37°C and 5% CO_2. Half of the media was changed at 7 DIV and once a week thereafter. Experiments were performed between 13 and 17 DIV. Media was not changed during treatment Chronic pharmacological treatments were at the following concentrations: TTX (Alomone): 1μM; FK506 (in DMSO, Fisher): 5 μM; KN-93 (Fisher): 4μM.

Electrophysiological recordings and analysis

All chemicals for solutions were purchased from Sigma-Aldrich unless otherwise noted. Whole-cell voltage-clamp recording of miniature excitatory postsynaptic currents (EPSCs) were conducted from 13 to 17 days *in vitro* (DIV). Recordings were performed at 33°C in 4K Tyrode's solution: NaCl 150mM, KCl 4mM, HEPES 10mM, Glucose 10mM, $MgCl_2$ 2mM, $CaCl_2$ 2mM, at 7.40 pH, with 1μM tetrodotoxin (TTX, Alomone Labs) and neurons clamped at −65mV. Internal voltage clamp solutions: 135 $CsMeSO_4$ 135 mM, KCl 5mM, $MgCl_2$ 4mM with ATP Buffer: HEPES 10mM, EGTA 0.3mM, Tris-Phosphocreatine 10mM, Mg-ATP 4 mM, Na-GTP 0.3mM, pH to 7.35 with KOH. Recordings were not corrected for liquid junction potential. Recorded neurons were rejected if they did not meet the following criteria: $V_{rest} < -50$mV, $R_{access} < 20$ MΩ with <33% change throughout the recording, and >900μs membrane decay constant. Acute profusion of 10μM philanthotoxin (Cayman Chemical Company) was conducted for up to 10 min after 5 min of baseline recording. Analysis of electrophysiology recordings were conducted with molecular devices ABF files imported into MATLAB. Openly available import functions can be found: abfload.m (Forrest Collman, 2009), detectPSPs.m (Phil Larimer, 2007). mEPSCs were detected after lowpass filtering and with an event threshold minimum of 5pA. For each event, amplitude was measured by taking the peak of an event, and instantaneous frequency by inverting the interevent interval (IEI) of the previous event. Decay τ constants were calculated by fitting each individual event from peak to baseline with a decaying exponential function. Plotted averages were taken from the mean of the mean of each recorded cell. Empirical cumulative distributions were calculated for each condition, normalized to the number of events for each cell. All scripts and data are available on a public repository, linked in the Key Resources Table.

Imaging

For immunofluorescence of pCaMKII, αCaMKII, and βCaMKII (Figure 5), cells were fixed in ice-cold 4% paraformaldehyde in phosphate buffer with 20 mM EGTA and 4% sucrose, permeabilized with 0.1% Triton X-100 and blocked with 10% normal donkey serum or 10% bovine serum albumin; and incubated overnight at 4°C in primary antibodies. For surface staining of GluA1 (Figure 3), coverslips were fixed and blocked in 10% normal donkey serum or 10% bovine serum albumin for 30 min in the absence of Triton X-100. Surface staining with primary GluA1 antibodies was then performed for 1 h at room temperature. Cells were then permeabilized in 0.1% Triton X-100, and stained with anti-PSD-95 and anti-MAP2 overnight at 4°C. For secondary antibodies, cells were washed with PBS (3 × 5 min), incubated at RT for 40 min with Alexa secondary antibodies (1:1000, Molecular Probes), washed again with PBS (3 × 5 min) and mounted with ProLong Gold + DAPI (Invitrogen).

Fixed immunostained cells were imaged with a 63× oil objective on a Zeiss LSM 800 confocal microscope at 2048 x 2048 resolution. Z-stacks were taken such the layer of dendrites was within the full Z-range (approximately 3–5 μm). At least two biological replicates were taken for each experimental timepoint and genotype. Maximum intensity z-projections were created with the open-source bioimaging program suite ICY with the Zeiss microscopy software package were then created for image analysis. All intensity quantification was performed using ICY. ROIs were drawn using the following criteria: MAP2 staining was present

with PSD-95 puncta that were juxtaposed with channel to be measured (ex. GluA1, pCaMKII, etc) blinded. Approximately 30–50 ROIs were taken from each maximum intensity projection. A region of interest lacking soma or neurites was selected in each maximum intensity projection as background, and the mean intensity was then subtracted from all intensity measurements from that field of view.

In immunohistochemical experiments (Figures 3, 5, S4, S6 and S7) each data point reflects the mean signal intensity of interest (surface GluA1, pCaMKII, αCaMKII, βCaMKII) within PSD-95 puncta in a dendritic segment. Puncta in the PSD-95 channel were identified using ICY's spot detector tool with the following settings: UDWTWaveletDetector, bright spot over dark background, scale 2, sensitivity 100, ∼3 pixels, without filtering. The region without PSD-95 puncta within an ROI was designated as shaft. The mean intensity was measured, giving two mean intensity measurements for each ROI: synaptic (within PSD-95 puncta) and shaft (not in PSD-95) puncta. ROI measurements from each replicate were combined for each timepoint. Mean intensities were then imported into MATLAB and Graphpad Prism to conduct statistical analyses and data visualization.

QUANTIFICATION AND STATISTICAL ANALYSIS

Statistical tests for group effects

Statistical analyses and tests were performed using Graphpad Prism (versions 8, 9, and 10) and MATLAB. Ordinary one-way ANOVAs were used to compare WT experiment, Figure 1 with two-sided comparisons and corrections. Ordinary two-way ANOVAs were used to compare group means with regard to genotype (WT, TiS) and hours of chronic drug treatment (TTX, FK506, KN93) and interactions. Two-sided comparisons were always conducted with multiple comparison corrections (Tukey correction for comparisons between TTX timepoints within genotype, and Sidak correction for TTX timepoints across genotypes) unless otherwise noted. For PhTx experiments, mEPSCs were aggregated in minute bins, and aligned to time of drug application. Times before drug application were labeled as baseline. For +/− PhTx comparisons, the 3 min preceding drug application were binned as "baseline", the last 3 min were binned as "+PhTx". F values and degrees of freedom are reported in main text, figures, and supplemental tables. Statistical significances are indicated with *p < 0.05, **p < 0.01, etc. and are detailed in each figure legend and in the supplementary tables. Data is represented as mean ± SEM. Number of samples, test results, and corresponding p values can be found in figures and main text, with full reports in supplemental figures and Tables S2–S8.

Linear regression

Linear regression fits by least-squares were conducted using MATLAB's mldivide function or '\' operator to identify the regression coefficient. Datasets were structured such that a given condition and timepoint, that one mean measurement (i.e., mean Deacy Tau or mean synaptic GluA1 in Figure 3) as the independent variable and the other (i.e., mean mEPSC amplitude) as the dependent variable. R^2 values were calculated by: $R^2 = 1 - \frac{\sum_{i=1}^{n}(y_i - \widehat{y_i})^2}{\sum_{i=1}^{n}(y_i - \overline{y_i})^2}$

Model supplement
Model definition

We modeled the average concentration of postsynaptic calcium, Ca, represented on a log scale as $\log Ca$, treating it as the combination of a baseline level of calcium Ca_0, and quantal rate-mediated increments in calcium through synaptic GluA1-independent and GluA1-dependent sources,

$$\log Ca = \log [Ca_0 + Ca_{PSP0}R + \overline{Ca}_{GluA1}RA] \qquad \text{(Equation 1)}$$

where R is the total rate of quantal delivery in Hz (including both spontaneous PSCs (minis), and evoked EPSCs), Ca_{PSP0} is the calcium from PSCs at 1 Hz, A is the proportion of GluA1 that has been phosphorylated and trafficked to the synapse, and $\overline{Ca}_{GluA1}$ is the maximal calcium provided by GluA1 from PSCs at 1 Hz (i.e., when $A = 1$). Ca_{PSP0} and $\overline{Ca}_{GluA1}$ were chosen to give a plausible dynamic range of calcium levels at physiological quantal rates. This simple summation of contributions from various calcium sources is a first approximation, ignoring possible non-linear dependence of restorative processes on Ca. This expression is also repeated as the first equation in main text.

GluA1 activation by a combination of membrane insertion and C-terminal phosphorylation[20] was modeled as a kinetic equation

$$\dot{A} = k_f(1 - A) - k_d A \qquad \text{(Equation 2)}$$

in which k_f is the rate of phosphorylation set by protein kinase activity and k_d is the rate of dephosphorylation due to protein phosphatase activity (Equation S1).

$$k_f = k_{f_0} + \overline{k}_{CaMK}m$$

$$k_d = k_{d_0} + \overline{k}_{CaN}n$$

where k_f and k_d were elevated by the calcium-dependent activation of CaMKII and CaN, respectively, over and above a calcium-independent baseline level, where k_{f_0} and k_{d_0} designate the baseline (Ca^{2+}/CaM-independent) levels of CaMKII and CaN activity, respectively.

Further, m and n are dynamic variables representing the activation level of CaMKII and CaN, and $\overline{k}_{CaMK}$ and $\overline{k}_{CaN}$ are the corresponding maximal dynamic ranges.

The dynamics of the m and n gates were each modeled by a first order differential equation,

$$\tau_x \frac{dx}{dt} = -x + x_\infty(\log Ca)$$

$$x_\infty(\log Ca) = \left(1 + e^{S_x(\log Ca - \log Ca_x)}\right)^{-1} \quad x \in \{m, n, b\}$$

with time constant tau, and sigmoid activation functions that define steady state for each gate as a function of log Ca.

The CaMKII activation function was further modulated by a variable, b, that represents the proportion of the β isoform, such that with 100% βCaMKII, the m activation was more sensitive to calcium by a shift in log Ca-dependence, based on results from Brocke et al., 1999 and Thiagarajan et al., 2002.

$$\log Ca_m = \log Ca_\alpha - bCa_{\Delta b}$$

The parameters for αCaMKII and CaN activation functions were chosen to match experimental results of Brocke et al., 1999 and Stemmer and Klee, 1994 respectively. The ratio of k_{f_0} and $\overline{k}_{CaN}$ determined the steady-state value of Calcium, la (R) (Figure 7B), and was chosen so that the steady-state curve was relatively flat at around −7, i.e., such that for a wide range of quantal rate, physiological calcium was maintained by the balance of CaN and kinase activity. k_{f_0}, $\overline{k}_{CaMK}$, and $\overline{k}_{CaN}$ were further constrained by the ability to reproduce two additional features observed in the experimental data (Figure S10): an exponentially decaying $A(t)$ following reduction in (mimicking FK506 application, see also Figure 7), and the presence of an overshoot peak in $A(t)$ following the reduction of presynaptic rate (mimicking TTX application). All parameter values used can be found in Table S1.

The effects of Timothy syndrome were modeled by increasing Ca_{PSP0} by a factor of 1.2 and increasing log Ca_m by 0.1.

Steady state response

The steady state response of the model to presynaptic rate (Figures 7C, S9A and S9B) was solved by rearranging Equation 1 to separate R from terms containing pCa, and fixing the value of A under various conditions.

$$\frac{10^{-\log Ca} - Ca_0}{Ca_{PSP0} + \overline{Ca}_{GluA1} A} = R$$

Namely, we compared the case with $A = 1$ (CPARs maximally active and conductive), $A = 0$ (no CPARs), and A set to a steady state value determined by the calcium dependent phosphokinetic gates $A = \frac{k_f}{k_f + k_d} = \frac{k_{f_0} + \overline{k}_{CaMK} m}{k_{f_0} + \overline{k}_{CaMK} m + k_{d_0} + \overline{k}_{CaN} n}$ with each model component successively added as outlined below.

1. CaN-only: $n = n_\infty(\log Ca) \ m = 0$

2. CaN + αCaMKII: $n = n_\infty(\log Ca) \ m = m_\infty(\log Ca)$

3. CaN + α/βCaMKII $n = n_\infty(\log Ca) \ m = m_\infty(\log Ca + Ca_{\Delta b} b_\infty(\log Ca))$

Presynaptic oscillation

The presynaptic oscillation was modeled using a decaying oscillation,

$$R(t) = \begin{cases} R_{eq} - R_0 e^{\frac{-t}{\tau}} \cos\left(\frac{2\pi(t+\varphi)}{T_0 + Tt_s}\right), x \geq 0 \\ R_{spont}, x < 0 \end{cases}$$

With parameters fit to the experimentally observed time course ($R_{eq} = 26.0$; $R_0 = 15.95$; $\tau = 40.11$hr; $T_0 = 15.08$hr; $T_s = 0.35$ $\varphi = -0.59$) using the fit function in MATLAB.

Model limitations

(1) We model a single postsynaptic spine as representative of all such spines, ignoring possible heterogeneity among them arising from competition of enzymatic or vesicular resources, as well as spatial variations in intracellular calcium. (2) We treat the presynaptic input as a continuous variable R, representing the rate of quantal delivery regardless of whether it is evoked release or spontaneous

release, effectively disregarding spike timing when spikes occur (relevant to graded reductions in *R*). (3) We focus on CaN as the main GluA1 phosphatase and CaMKII as the chief kinase, ignoring possible contributions from other related protein phosphatases and kinases. (4) We linearize calcium regulation, thereby ignoring saturation phenomenon such as calcium buffering or calcium activation of Ca^{2+} pumps, and (5) we treat CaMKII as a hybrid of the known properties of its α and β isoforms, acknowledging their different sensitivities to Ca^{2+}/CaM while ignoring possible heterogeneity across individual holoenzymes.

Further, because the experimental protocol was limited to repeated samples of a small number of timepoints (rather than densely sampling at different timepoints), fitting the exact dynamics is highly sensitive to overfitting, as well as the conversion factor from mini amplitude to the exact value of *A*. Thus, we were unable to directly fit the timecourse of the model to the experimental data. However, we performed a hyperparameter sweep to demonstrate that the qualitative results of the model are relatively robust and emerge for a range of hyperparameter values (Figure S10).